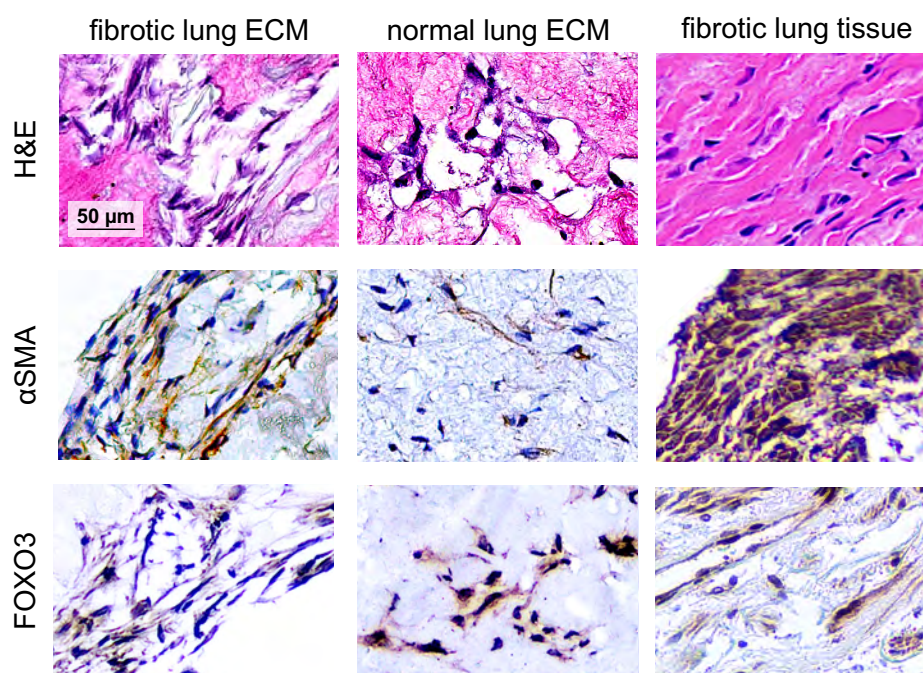# Fibrotic human lung extracellular matrix as a disease-specific substrate for 3D *in-vitro* models of pulmonary fibrosis

Igal Germanguz[†], Evelyn Aranda[†], Jennifer C. Xiong, Natalia Kissel,

Alexandra Nichols, Eddie Gadee, John D. O'Neill*

Xylyx Bio, Inc.
760 Parkside Avenue
Brooklyn, New York 11226, USA

[†] Authors contributed equally

* Correspondence: John D. O'Neill, Email: john@xylyxbio.com

1   **Fibrotic human lung extracellular matrix as a disease-specific substrate for 3D *in-vitro***

2   **models of pulmonary fibrosis**

3

4   Igal Germanguz[1†], Evelyn Aranda[1†], Jennifer C. Xiong[1], Natalia Kissel[1], Alexandra Nichols[1], Eddie

5   Gadee[1], John D. O'Neill[1]*

6

7   [1] Xylyx Bio, Inc., 760 Parkside Avenue, Brooklyn, New York 11226, USA

8   [†] Authors contributed equally

9   * Correspondence: John D. O'Neill, Email: john@xylyxbio.com

10

11   **ABSTRACT**

12   Idiopathic pulmonary fibrosis (IPF) is an irreversible and uniformly fatal lung disease marked by

13   destruction and scarring of the lung parenchyma and progressive loss of respiratory function. IPF

14   affects nearly 3 million people worldwide, and annual mortality in the US alone exceeds 40,000.

15   Nintedanib and pirfenidone, the only drugs approved for the treatment of IPF, slow progression

16   but do not cure the disease. Consequently, there is a pressing need for effective treatments

17   beside lung transplantation. Unfortunately, predictive models of IPF are not available,

18   underscoring the critical need for physiologically relevant *in-vitro* substrates that enable

19   quantitative and mechanistic studies of human IPF. Here we report the development and

20   characterization of a human pulmonary fibrosis-specific cell culture substrate comprised of intact

21   fibrotic lung extracellular matrix that recapitulates the human IPF disease environment *in vitro*.

22   We document the activation and disease-specific phenotype of human lung fibroblasts cultured

23   in the IPF disease-specific substrate, and establish feasibility of testing antifibrotic agents using

24   this substrate. Altogether, our results demonstrate the applicability of this fibrosis-specific

25   substrate for 3D *in-vitro* models of IPF and cell-based assays in early-stage drug discovery.

26   **Keywords:** 3D cell culture, drug testing, extracellular matrix, idiopathic pulmonary fibrosis, *in-*

27   *vitro* models, lung disease, lung fibroblasts, scaffolds

28   **INTRODUCTION**

29   Idiopathic pulmonary fibrosis (IPF) is a chronic interstitial lung disease that primarily affects older

30   adults and is associated with dysregulation of pulmonary fibroblasts, extensive remodeling and

31   deposition of extracellular matrix, and progressive loss of respiratory function.[1-3] Incidence and

32   prevalence appear to be increasing worldwide with aging populations and improved diagnostics.[4]

33   Every year more than 50,000 new patients are diagnosed with IPF[5] – an incidence comparable

34   to those of liver, stomach, testicular, or cervical cancers.[6] After diagnosis, median survival is only

35   3 – 4 years, and annual mortality exceeds 40,000.[7] The etiology of IPF remains unknown, but risk

36   factors include smoking, environmental exposures, chronic viral infections, gastroesophageal

37   reflux, lung injury, and genetic predispositions.[4,8] Nintedanib and pirfenidone, the only drugs

38   approved to treat IPF, attenuate disease progression but do not prevent decline,[1,4,9] necessitating

39   the development of new drugs that can effectively treat IPF.

40

41   A major obstacle to developing effective treatments for IPF is the lack of predictive animal and *in-*

42   *vitro* models of IPF. Animal models of pulmonary fibrosis are well-established in rodents[10-12] but

43   present fibrosis that resolves over time rather than the progressive, non-resolving fibrotic process

44   characteristic of IPF in humans.[3,13] Furthermore, there are no robust or widely adopted *in-vitro*

45   models of IPF to enable predictive basic and translational studies.[14] Consequently, an *in-vitro*

46   model of IPF that emulates human pathophysiology could enable critical new insights into the

47   natural history and pathological mechanisms of IPF, and guide therapeutic development.
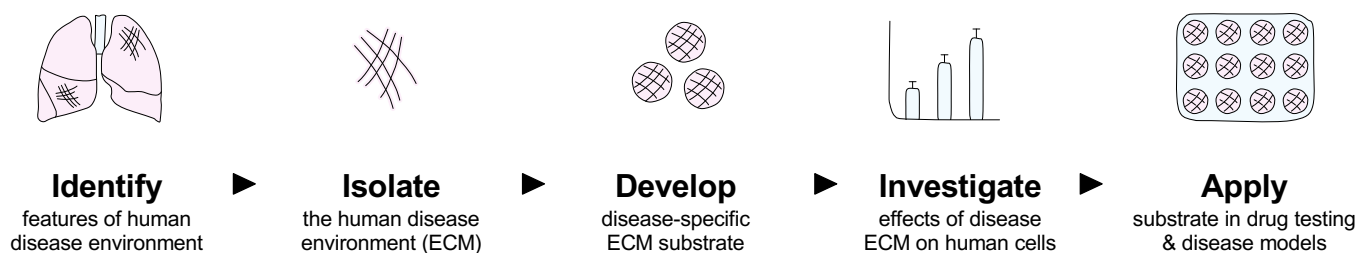
48

49   Current *in-vitro* models of IPF have limited physiologic relevance because they fail to recapitulate

50   the complex biochemical, structural, and mechanical environment of fibrotic human lungs. In

51   fibrosis, the extracellular matrix (ECM) has different biochemical composition, stores more

52   fibrogenic growth factors, and has altered structure and biomechanics compared to normal

53   ECM,[15-17] and the direct influence of growth factors[18,19] and increased matrix stiffness[20] on

54   myofibroblast differentiation has been previously demonstrated. Altogether, such matrix

55   alterations induce a profibrotic microenvironment, activate pulmonary fibroblasts, and suggest

56   that IPF progression is correlated with an abnormal ECM microenvironment.[21] As lung matrix is

57   implicated in both lung function and fibrotic disease progression, IPF models and drug screening

58   platforms not incorporating lung ECM lack defining components of the IPF disease environment.

59   The most common *in-vitro* IPF drug testing platforms utilize cell culture plates coated with collagen

60   type I and culture media supplemented with high concentrations of transforming growth factor β

61   (a profibrotic cytokine associated with fibrogenesis),[22] but no testing platforms that utilize other

62   IPF disease-specific ECM components have been established.

63

64   An *in-vitro* cell culture substrate comprised of fibrotic human lung matrix could faithfully

65   recapitulate the composition, structure, and mechanics of the human IPF disease environment.

66   While removal of native cells (decellularization) from human tissues has been demonstrated in a

67   number of tissues including lungs[23-26], efforts have been primarily focused on the isolation and

68   characterization of ECM from normal, non-diseased tissues. Reproducible, scalable methods for

69   the production of disease-specific ECM biomaterials from diseased human tissues such as fibrotic

70   lungs have not been robustly established. Furthermore, an *in-vitro* cell culture substrate that

71   recapitulates the complex disease environment of human IPF tissue would be an extremely

72   valuable tool for screening antifibrotic agents in early-stage development.

73

74   In this study, we investigated the feasibility of developing a cell culture substrate from fibrotic

75   human lung tissue for 3D *in-vitro* models of human pulmonary fibrosis. Our hypothesis was that

76   normal human lung fibroblasts would display a disease-specific phenotype *in vitro* in the presence

77   of fibrotic lung extracellular matrix. We implemented a 'physiomimetic approach' to develop

78   disease-specific IPF cell culture substrates (scaffolds) comprised of lung extracellular matrix

79   derived from human IPF tissues (**Fig. 1**). Our goal was to develop a human fibrotic lung ECM

4

Physiomimetic approach for development of disease–specific cell culture substrates

Identify	▶	**Isolate**	▶	**Develop**	▶	**Investigate**	▶	**Apply**
features of human disease environment		the human disease environment (ECM)		disease-specific ECM substrate		effects of disease ECM on human cells		substrate in drug testing & disease models

Figure 1 | Overview of physiomimetic approach. Our development of IPF disease-specific cell culture substrates is guided by a physiomimetic approach that aims to identify and isolate the human disease environment, then develop and investigate disease-specific ECM substrates *in vitro* utilizing disease-relevant human cell types (e.g., pulmonary fibroblasts) whose phenotype can be directly compared against diseased human IPF lung specimens prior to application in IPF disease models and antifibrotic drug testing.

80   biomaterial for use as a 3D cell culture substrate for predictive *in-vitro* models of IPF that could

81   reduce dependence on animal models while enabling physiologically relevant results. Such

82   disease-specific cell culture substrates could radically improve the physiological relevance of *in-*

83   *vitro* models of IPF and antifibrotic drug screening platforms, and accelerate development of safe

84   and effective IPF treatments.

85

86   **MATERIALS & METHODS**

87

88   **Procurement of human lung tissues.** Acceptance criteria for donors of normal and IPF lungs

89   were established prior to initiation of studies. Normal lung donors had no history, diagnosis, or

90   evidence of: smoking, aspiration pneumonia, asthma, chronic obstructive pulmonary disease,

91   cystic fibrosis, emphysema, interstitial lung disease, or lung cancer. IPF donors required

92   diagnosis of idiopathic pulmonary fibrosis confirmed by a lung transplant pathologist. All IPF

93   donors had end-stage disease and were recipients of lung transplants. Normal human lungs (n =

94   3) not acceptable for use in transplantation were procured under a protocol approved by the

95   Institutional Review Board at the International Institute for the Advancement of Medicine.

96   Diseased human lungs (n = 3) designated as surgical waste were procured under protocols

97   approved by the Institutional Review Boards at Vanderbilt University Medical Center and State

98   University of New York (SUNY) Downstate Medical Center. Lungs were procured in standard

99   fashion, flushed with cold organ preservation solution, transported on ice, and made available

100   without identifiers. In this study, to minimize variability, lung tissues from right middle and right

101   lower lobes were utilized.

102

103   **Characterization of lung donors.** Lung donor characteristics were tabulated from deidentified

104   summaries provided by the United Network of Organ Sharing (UNOS) under approved protocols

105   and in compliance with all applicable regulations.

5

106 **Sampling of lung tissues.** Tissue samples were collected from medial, lateral, and peripheral

107 regions of right middle lobes (2 samples per region), for a total of 6 regional samples per right

108 middle lobe, and 18 regional samples each for IPF and normal lungs.

109

110 **Preparation of lung matrix scaffolds.** Upon receipt, lungs were rinsed with cold sterile saline.

111 Native lung tissue samples were collected for histologic analyses, then lung tissues were stored

112 at −80°C. At the time of use, lung tissues were processed under sterile conditions with a

113 proprietary combination of chemicals, enzymes, and surfactants to remove cellular components

114 and isolate normal and fibrotic lung extracellular matrix. Matrix scaffolds (diameter: 7 mm,

115 thickness: 1 mm) were prepared under sterile conditions for experimental use. For all assays,

116 three tissue samples or matrix scaffolds were randomly selected from each lung and evaluated in

117 triplicate.

118

119 **Histologic analyses of lung tissues and scaffolds.** Lung tissue samples were fixed in cold

120 phosphate-buffered 4% paraformaldehyde for 24 hours, embedded in paraffin, and sectioned at

121 5 or 10 μm thickness. Three sections (medial, lateral, peripheral) from all normal and fibrotic lungs

122 were stained with hematoxylin and eosin, trichrome, Verhoeff–Van Gieson, Alcian blue, and

123 pentachrome, and examined under light microscopy. Representative images were obtained using

124 a fluorescence microscope (FSX100, Olympus).

125

126 **Histopathologic characterization of lung tissues.** All lung sections were subjected to blinded

127 review by a lung transplant pathologist. Slides were randomized, arbitrarily numbered, and

128 delivered without reference to the pathologist, who reviewed and assigned fibrosis scores to all

129 regions in 5 high-power fields according to a standard pulmonary fibrosis scoring rubric[27] to

130 quantify the extent of architectural disruption and fibrosis (**Supplementary Fig. 1C**). Fibrosis

131 scores from each high-power field were averaged to obtain an average fibrosis score for each

6

132 region of lung. To quantitatively assess the severity and distribution of fibrosis, a grid with unit

133 length 250 μm was overlaid onto each high-power field (20×) image, and regions corresponding

134 to various classifications of fibrosis were outlined (**Supplementary Fig. 1F**). Each region was

135 assigned a calculated relative percent area of the high-power field using the grid. Each fibrosis

136 score was weighted according to percent area, and average fibrosis scores for each high-power

137 field were calculated based on the weighted average of all regional fibrosis scores in each high-

138 power field. Fibrosis scores were then averaged across 5 high-power fields per region, with four

139 regions evaluated per lobe. Only regions of IPF lungs with confirmed fibrosis score ≥ 2 were

140 investigated in this study (**Supplementary Fig. 1D,E,G**).

141

142 **Biochemical characterization of lung tissues and scaffolds.** To quantify collagen in lung

143 tissues and scaffolds, samples were weighed, homogenized, and digested with pepsin (0.1 mg

144 mL^{-1}) in 0.5M acetic acid for 12 hours at 4°C, and subjected to a collagen quantification assay

145 (Sircol, Biocolor) according to the manufacturer's instructions. To quantify sulfated

146 glycosaminoglycans in lung tissues and scaffolds, samples were weighed, homogenized, and

147 digested with papain (1 μg mL^{-1}) for 12 hours at 60°C, and subjected to the dimethylene blue dye

148 assay, wherein absorbance was measured at 595 nm. To quantify elastin in lung tissues and

149 scaffolds, samples were weighed and homogenized, and soluble α–elastin was extracted via

150 three extractions with hot 0.25M oxalic acid. Samples were then subjected to an elastin

151 quantification assay (Fastin, Biocolor) according to the manufacturer's instructions. To quantify

152 residual DNA in matrix scaffolds, samples were subjected to a quantitative DNA assay (Quant-iT

153 PicoGreen, Invitrogen) according to the manufacturer's instructions.

154

155 **Immunohistochemical staining.** Following de-paraffinization, sections of lung tissues and

156 scaffolds were subjected to boiling citrate buffer (pH 6.0) for antigen retrieval, and blocked with

157 5% normal goat serum in phosphate-buffered saline for 1 hour at room temperature. Next,

158 antibodies were diluted as necessary, applied, and incubated for 12 hours at 4°C or 4 hours at

159 room temperature. Sections were mounted (VectaMount Permanent Mounting Medium, Vector

160 Laboratories), and coverslips were applied. Images were obtained using a light microscope

161 (Eclipse Ts2, Nikon). Immunohistochemical stains were performed for alpha smooth muscle actin

162 (Cell Signaling Technology, 19245), fibrillin 2 (Sigma Life Science, HPA012853), Ki67

163 (ThermoFisher Scientific, PA1-38032), laminin γ1 (Abcam, ab233389), matrix gla protein (LS Bio,

164 LS-B14824), and periostin (Abcam, ab14041). A list of antibodies with dilutions used is provided

165 in **Supplementary Table 1**.

166

167 **Quantification of immunohistochemical staining by image analysis.** Images of immuno-

168 histochemical stains were captured using a slide scanner (P250 High Capacity Slide Scanner, 3D

169 Histech). To quantify immunohistochemical staining, images were analyzed using an image

170 analysis software module (DensitoQuant, Quant Center, 3D Histech), and the number of positive

171 and negative pixels were quantified and analyzed.

172

173 **Mass spectrometry of IPF and normal lung matrisomes**. Detailed methods are available in the

174 Supplementary Information.

175

176 **Quantification of growth factors.** To quantify growth factors in native lung tissues and matrix

177 scaffolds, a multiplex growth factor array (Quantibody Human Growth Factor Array Q1; Ray

178 Biotech) was performed and analyzed by Q-Analyzer software. To quantify growth factors

179 secreted by human fibroblasts *in vitro*, enzyme-linked immunosorbent assays (ELISA) were

180 performed for bFGF (R&D Systems, DFB50) and TGFβ (R&D Systems, DB100B). All samples

181 were analyzed in triplicate.

182   **Scanning electron microscopy.** Lung matrix samples were collected, fixed in formalin for 24

183   hours, rinsed in 70% ethanol, frozen, lyophilized, and imaged using an electron microscope

184   (GeminiSEM 300, Zeiss) with accelerating voltage 2.5 kV.

185

186   **Transmission electron microscopy.** Lung matrix samples were fixed with 2.5% glutaraldehyde,

187   4% paraformaldehyde, and 0.02% picric acid in 0.1M Na-cacodylate buffer (pH 7.2). Samples

188   were then post-fixed with 1% OsO4 in Sorenson's buffer for 1 hour, dehydrated, and embedded

189   in Lx-112 (Ladd Research Industries). Sections (thickness: 60 nm) were prepared using a PT-XL

190   ultramicrotome, stained with uranyl acetate and lead citrate, and examined with an electron

191   microscope (JEM-1200 EXII; JEOL). Images were captured with a digital camera (ORCA-HR;

192   Hamamatsu Photonics) and recorded with imaging software (Image Capture Engine, AMT).

193

194   **Mechanical testing of IPF and normal lung scaffolds.** Uniaxial tensile mechanical testing was

195   conducted with a 10 N load cell (Model 5848, Instron), as previously described.[23] Lung tissues

196   and matrix from transverse sections of the right middle lobe were randomly selected and

197   dissected into 3 cm by 1 cm samples. A consistent orientation from right middle lobe was

198   maintained to minimize effects of lung anisotropy on mechanical testing data. Samples were

199   secured and mounted, and a pre-load of 0.003 N was applied. All samples were tested at the

200   same grip-to-grip distance for consistency. Samples were kept hydrated throughout all

201   mechanical testing with phosphate-buffered saline at room temperature. A 20% uniaxial strain

202   was applied at a strain rate of 1% s^{-1}, and at frequencies of 0.25, 0.50, or 0.75 Hz.

203

204   **Cell culture.** Human lung fibroblasts (ATCC) were cultured in Dulbecco's Modified Eagle Medium

205   (DMEM) supplemented with 10% fetal bovine serum and 1% penicillin/streptomycin under

206   standard culture conditions with 5% CO_2 at 37ºC.

9

207   **Gene expression analysis.** Total RNA was extracted (RNeasy Micro Kit, QIAGEN), and cDNA

208   synthesis was performed using random primers (iScript Select cDNA Synthesis Kit, Bio-Rad).

209   Quantitative real-time polymerase chain reaction (qPCR) was performed in triplicate using master

210   mix (Brilliant III Ultra-Fast SYBR Green QPCR Master Mix, Agilent Technologies) and a real-time

211   PCR system (AriaMax Real PCR System, Agilent Technologies). A list of primers is provided in

212   **Supplementary Table 2**.

213

214   **Drug testing.** Normal human fibroblasts were cultured *in vitro* for 24 hours, then exposed to

215   antifibrotic agent PF3644022 hydrate (PZ-0188, Sigma-Aldrich) at a concentration of 1 µM for 72

216   hours. Metabolic activity was measured using Alamar Blue reagent (DAL1025, ThermoFisher

217   Scientific) according to the manufacturer's instructions. The reagent was added to cells in culture

218   at 24, 48 and 72 hours, and incubated for 4 hours before readout. Absorbance was measured at

219   570nm, with reference wavelength at 600 nm.

220

221   **Statistical analyses.** One-way ANOVA and Student's *t*-tests were performed using statistical

222   analysis software (Prism 8, GraphPad), and $p < 0.05$ was considered significant.

223

224   **RESULTS**

225

226   **Assessment of IPF and normal lungs.** Donor characteristics of IPF and normal lung tissues

227   were analyzed to confirm that there were no significant differences in age, height, weight, body

228   mass index, or smoking history (**Supplementary Fig. 1A,B; Supplementary Table 3**). An

229   established numerical rubric[27] was used to assess the extent of histomorphologic disruption and

230   fibrosis. Tissue sampling and histopathologic analyses are described in detail in Supplementary

231   Information.

10

232 **Preparation of lung matrix scaffolds.** Native lung tissues were treated with a proprietary

233 combination of chemicals, enzymes, and surfactants to remove cellular and nuclear components,

234 which was confirmed by hematoxylin and eosin staining (**Fig. 2A**) and quantitative DNA assay

235 (**Supplementary Fig. 2A**). Matrix scaffolds from all human lungs were confirmed negative for

236 mycoplasma, bacteria, and fungi (**Supplementary Fig. 2B**), and deemed suitable for use in cell-

237 based studies.

238

239 **IPF matrix scaffolds recapitulate disease-specific histologic features.** For histologic

240 evaluations of IPF, representative fields corresponding to fibrosis score 3 (severe fibrosis) were

241 selected. To visualize distributions of ECM structural components in IPF and normal lungs,

242 histologic staining was performed on native (untreated) tissues and matrix scaffolds. H&E staining

243 of native IPF tissues revealed severe distortion of lung structure and large areas of fibrous

244 obliteration with minimal remaining airspace (**Fig. 2A**). By contrast, H&E staining of native normal

245 lung tissues displayed abundant airspaces defined by thin alveolar septa and stereotypical

246 alveolar saccular architecture. Matrix scaffolds from analogous regions of IPF and normal lungs

247 had no discernible nuclei and displayed drastic differences in scaffold architecture consistent with

248 fibrotic and normal native lung tissues, respectively. Trichrome staining showed dramatic

249 deposition of collagens (blue) throughout regions of severe fibrosis (**Fig. 2B**). In IPF tissues and

250 scaffolds, collagen fibers were observed in densely aligned bundles and in loosely disorganized

251 networks; whereas in normal lung tissues and scaffolds, collagen was organized along alveolar

252 septa and within the interstitium. Verhoeff–Van Gieson (VVG) elastic staining showed a notable

253 loss of elastic fibers (black) in regions of IPF tissues and scaffolds with severe fibrosis, whereas

254 in normal lung tissues and scaffolds elastic fibers were dispersed homogenously throughout the

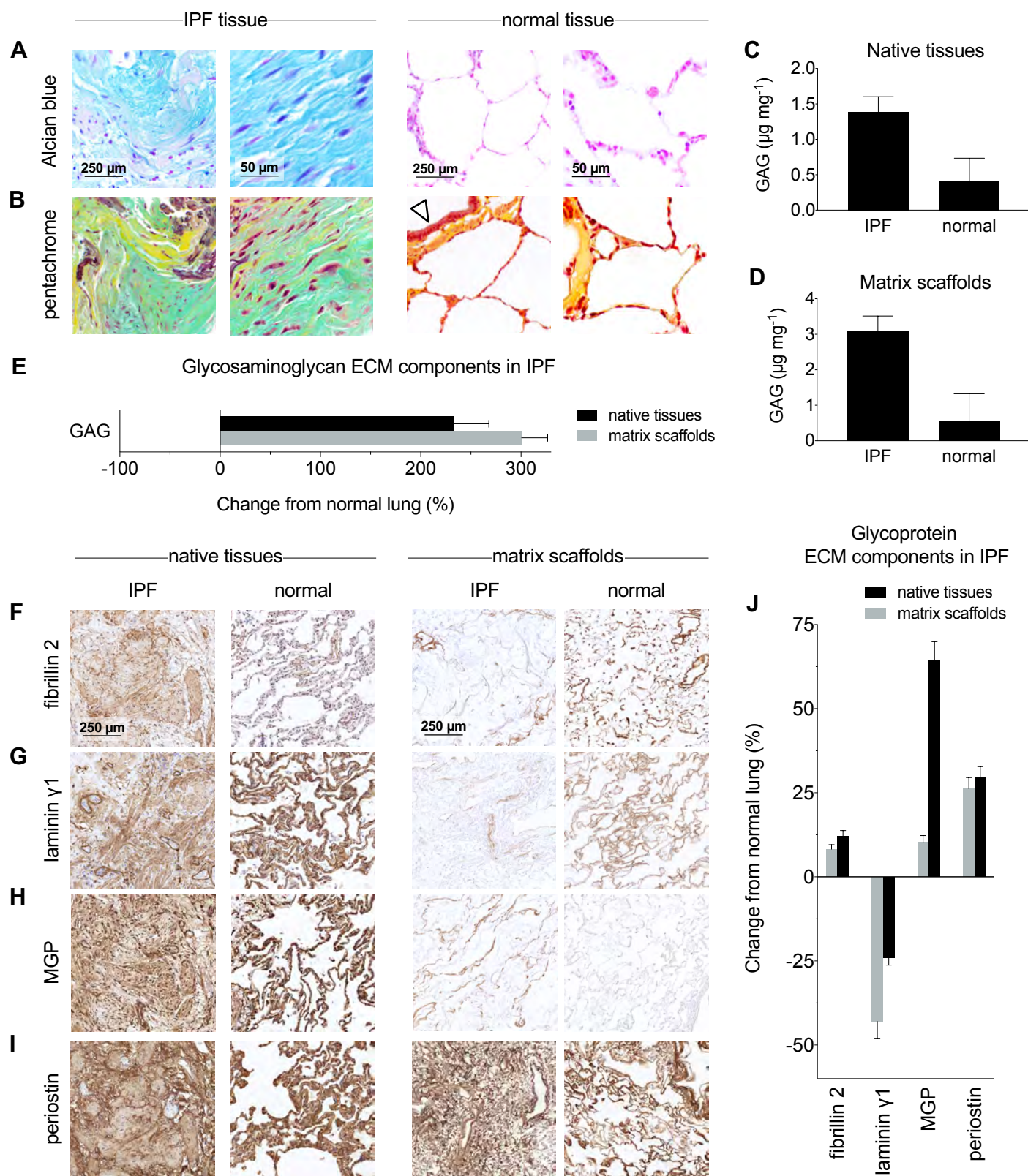255 respiratory zone (**Fig. 2C**).

256

11
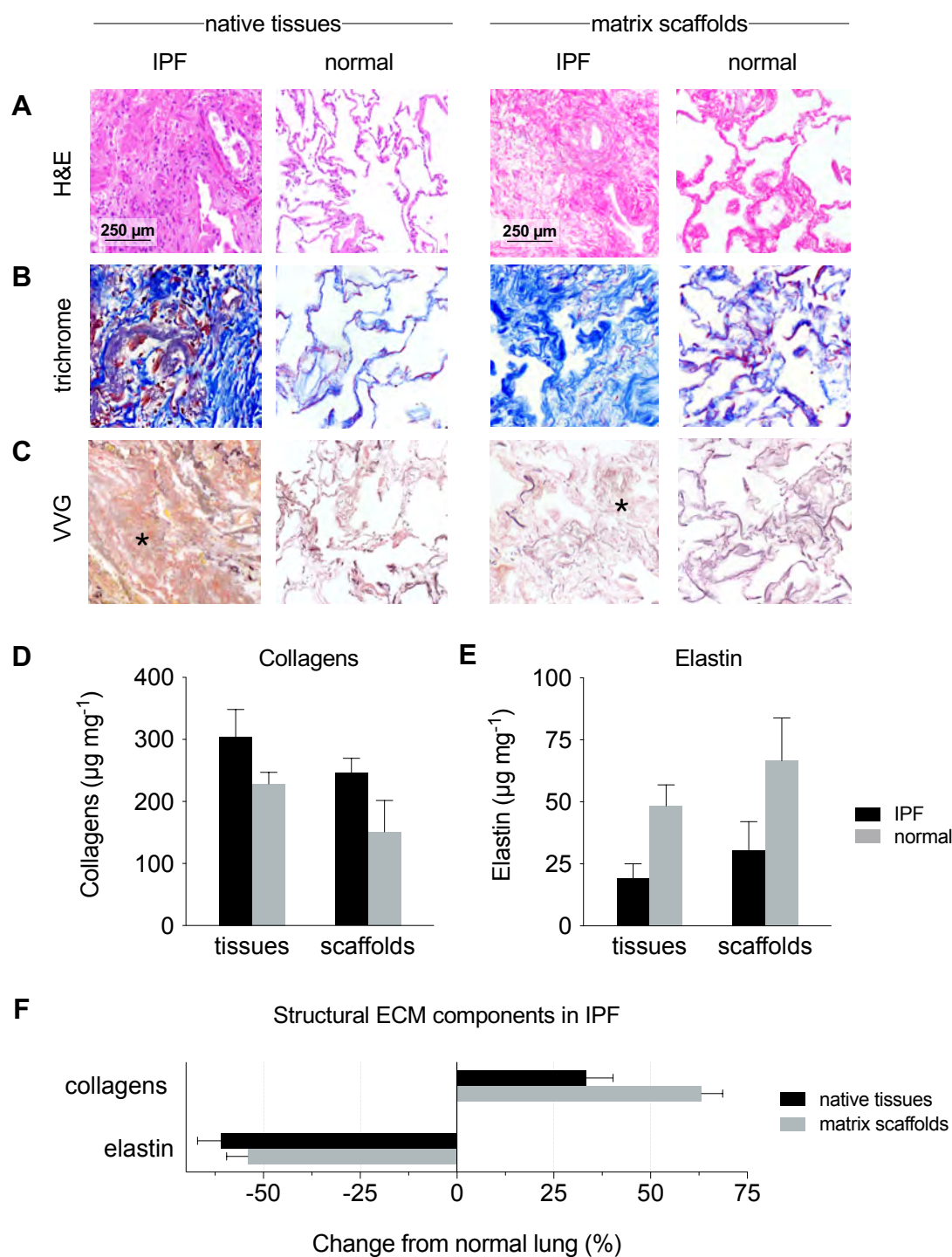
Figure 2 | Histologic & biochemical characterization of ECM structural components in IPF and normal lung tissues and matrix scaffolds. Representative micrographs of histologic stains: (**A**) hematoxylin and eosin (H&E), (**B**) trichrome (collagens, blue), and (**C**) Verhoeff–Van Gieson (VVG, elastic fibers, black) demonstrating differences in histomorphology of IPF and normal lung tissues and scaffolds. Star indicates representative region with severe fibrosis and loss of elastic fibers. Quantification of structural ECM components (**D**) collagens and (**E**) elastin by biochemical assays. (**F**) Changes from normal lung in structural ECM components in IPF. H&E: hematoxylin and eosin, VVG: Verhoeff–Van Gieson.

257   **IPF matrix scaffolds contain disease-specific biochemical composition.** Soluble collagens

258   were quantified in native tissues and matrix scaffolds, and increases in collagens were measured

259   relative to normal in IPF native tissues (33.3 ± 19.2 %) and matrix scaffolds (63.2 ± 15.6 %, **Fig.**

260   **2D**). Consistent with the loss of elastic fibers observed in VVG elastic staining, quantification of

261   elastin confirmed reduction in IPF native tissues (60.6 ± 12.3 %) and matrix scaffolds (54.1 ± 17.2

262   %) relative to normal (**Fig. 2E**). Altogether, the structural ECM components in IPF demonstrated

263   clear trends relative to normal in both native tissues and matrix scaffolds: increased collagens (33

264   – 63%) and decreased elastin (54 – 61%; **Fig. 2F**). Alcian blue and pentachrome staining were

265   performed to assess the extent and distribution of proteoglycans in IPF tissues, which was

266   significantly higher in areas of moderate and severe fibrosis (scores ≥ 2) than in areas of mild

267   fibrosis (scores < 2) and normal lung tissues (**Fig. 3A,B**). Quantification of sulfated

268   glycosaminoglycans (GAG) revealed that GAG components in IPF native tissues and scaffolds

269   was 232.5 – 300.5% higher than in normal lungs (**Fig. 3C-E**), consistent with overexpression of

270   sulfated glycosaminoglycans previously observed in fibrotic foci[28]. Immunohistochemical staining

271   of IPF tissues for multiple ECM glycoproteins revealed dramatic differences from normal lung

272   tissues in fibrillin 2, laminin γ1, matrix GLA protein (MGP), and periostin (**Fig. 3F-I**). Areas with

273   severe fibrosis (fibrosis score: 3) were characterized by pervasive overexpression of fibrillin 2,

274   MGP, and periostin, and loss of laminin γ1. Notably, changes from normal lung were consistent

275   in native tissues and matrix scaffolds for all glycoproteins that were investigated (**Fig. 3J**).

276

277   Mass spectrometry was performed on IPF and normal lung matrix scaffolds to assess the IPF

278   matrisome (**Table 1**), and revealed changes from normal lung consistent with histopathologic

279   observations and biochemical assays. Multiple collagen types increased above 150%, including

280   collagen types I, II, V, VI, VIII, XVI. Notably, in IPF lungs collagen types IV and XXI – the primary

281   collagens comprising the alveolar basement membrane – decreased between 33 – 73%,

282   consistent with the loss of basement membrane and alveolar structure associated with the

Figure 3 | Characterization of proteoglycans and glycoproteins in IPF lung tissues and matrix scaffolds. Representative micrographs of histologic stains: (**A**) Alcian blue (proteoglycans, blue) and (**B**) pentachrome (acidic polysaccharides, green) demonstrating differences in proteoglycans between IPF and normal lung tissues. Arrow indicates normal airway epithelium. Quantification of sulfated glycosaminoglycan ECM components in (**C**) native tissues and (**D**) matrix scaffolds. (**E**) Changes from normal lung in glycosaminoglycan ECM components in IPF. Immunohistochemical staining of glycoprotein ECM components in IPF: (**F**) fibrillin 2, (**G**) laminin γ1, (**H**) matrix gla protein (MGP), (**I**) periostin. (**J**) Quantification of glycoproteins by image analysis of immunohistochemical staining using DensitoQuant software.

Protein category	Description	Change from normal (%)	
Collagens	type II, α1 chain	5688.9	
	type XVI, α1 chain	511.1	
	type I, α1 chain	260.0	
	type VI, α3 chain	255.6	
	type VIII, α1 chain	202.3	
	type V, α1 chain	196.2	
	type I, α2 chain	188.2	
	type V, α2 chain	164.3	
	type VI, α2 chain	161.8	
	type VI, α1 chain	156.4	
	type I, α3 chain	139.0	
	type V, α3 chain	127.4	
	type IV, α2 chain	− 32.9	
	type IV, α1 chain	− 35.7	
	type IV, α3 chain	− 63.5	
	type IV, α5 chain	− 63.7	
	type IV, α4 chain	− 70.2	
	type XXI, α1 chain	− 72.9	
Glycoproteins	vitronectin	966.7	
	periostin	295.8	
	fibulin 2	222.2	
	laminin subunit α5	169.1	
	dermatopontin	107.7	
	laminin subunit β2	− 38.6	
	laminin subunit γ1	− 43.9	
	nidogen 1	− 52.8	
	laminin subunit α3	− 60.0	
Proteoglycans	biglycan	633.3	
	heparan sulfate PG core protein (BM-specific)	− 37.8	
Elastin	elastin isoform	− 31.1	
Matrisome secreted factors	hornerin	101.4	
ECM regulators	metalloproteinase inhibitor 3 (TIMP3)	637.5	
	cathepsin G	500.0	
	desmoplakin	414.3	
	serum albumin precursor	278.8	
	α1-antitrypsin	240	
	junction plakoglobin	202.9	
Immune factors	complement component C9	1422.2	
	immunoglobulin γ1 heavy chain	688.9	
	serum amyloid P-component	298.7	
	neutrophil defensin 3	− 28.1	
Keratin structural proteins	type I, cytoskeletal 9	259.4	
	type I, cytoskeletal 14	170.6	
	type II, cytoskeletal 2	167.2	
	type II, cytoskeletal 5	162.4	
	type I, cytoskeletal 10	149.8	
	type II, cytoskeletal 1	145.9	

%

300

250

200

150

100

50

0

-50

-75
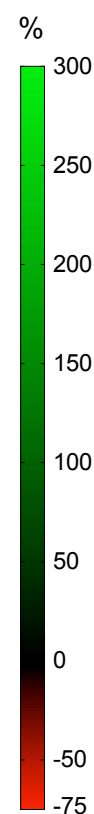
Table 1 | Mass spectrometry summary analysis of IPF lung matrisome. Changes from normal in the abundance of IPF lung matrisome components. PG: proteoglycan, BM: basement membrane,

283   progression of pulmonary fibrosis.[29] The glycoprotein vitronectin was elevated 967%, and

284   glycoproteins fibulin 2 and periostin were both elevated above 200%. Laminin subunits α3, β2,

285   γ1, and nidogen 1, which are associated with the basement membrane, were all decreased in IPF

286   lungs. Biglycan was increased by 633%, however basement membrane-specific heparan sulfate

287   proteoglycan core protein was decreased by 38%. Elastin isoforms were also decreased by 31%,

288   consistent with quantitative biochemical analyses. Interestingly, in IPF lungs several regulators of

289   the extracellular matrix were also increased more than 200% above normal, including

290   metalloproteinase inhibitor 3 (TIMP3), cathepsin G, desmoplakin, and α1-antitrypsin.

291

292   To assess changes in endogenous growth factors, a multiplex growth factor array was performed.

293   Two growth factors were detected only in IPF native tissues and not in normal lung native tissues:

294   transforming growth factor beta 3 (TGF-β3) and heparin-binding EGF-like growth factor (HB-EGF;

295   **Supplementary Table 4**). In IPF native tissues, insulin-like growth factor binding protein 1

296   (IGFBP-1) was 160-fold above normal, and both basic fibroblast growth factor (bFGF) and

297   endocrine gland-derived vascular endothelial growth factor (EG-VEGF) were approximately 20-

298   fold above normal. Brain-derived neurotrophic factor (BDNF) and growth differentiation factor 15

299   (GDF-15, a prognostic factor for IPF[30]) were elevated 3-fold to 5-fold, but osteoprotegerin (OPG)

300   was reduced by more than half. Five growth factors were detected in IPF matrix scaffolds (**Table

301   2**), including IGFBP-6, whose family of carrier proteins were shown to induce production of

302   collagen type I and fibronectin in normal primary lung fibroblasts[31,32]. Neurotrophin-4 (NT-4),

303   which is elevated in explanted IPF lungs and shown to drive proliferation of primary human lung

304   fibroblasts through TrkB-dependent and protein kinase B-dependent pathways[33], was also

305   detected in IPF matrix scaffolds.

306

307   **IPF matrix scaffolds have disease-specific structural and mechanical properties.** The gross

308   appearance of IPF matrix scaffolds was dramatically different from the appearance of normal lung

13

Growth factor	Description	Concentration (pg mL^{-1})		Fold change from normal
		Normal scaffold	IPF scaffold	
GDF-15	Growth differentiation factor 15	0.8	14.5	+ 18.1 ▲
BDNF	Brain-derived neurotrophic factor	6.3	48.7	+ 7.7 ▲
IGFBP-6	Insulin-like growth factor binding protein 6	14.1	71.8	+ 5.1 ▲
HGF	Hepatocyte growth factor	23.8	91.0	+ 3.8 ▲
EG-VEGF	Endocrine gland-derived vascular endothelial growth factor	0.6	1.5	+ 2.5 ▲
bFGF	Basic fibroblast growth factor	22.6	54.8	+ 2.4 ▲
HB-EGF	Heparin-binding EGF-like growth factor	1.4	2.5	+ 1.8 ▲
TGF-β3	Transforming growth factor β3	2.8	4.0	+ 1.4 ▲
VEGF	Vascular endothelial growth factor	4.6	3.0	− 0.3 ▼
EGF R	Epidermal growth factor receptor	ND	ND	–

Table 2 | Quantification of growth factors in IPF and normal lung matrix scaffolds. Growth factor concentrations were measured by multiplex growth factor array. Green arrow (▲) indicates positive fold change (increase) from normal in concentration of growth factors. Red arrow (▼) indicates negative fold change (decrease) from normal in concentration of growth factors. ND: not detected.

309   matrix scaffolds. Normal lung matrix scaffolds appeared translucent, with visible bronchial and

310   vascular conduits and saccular structures throughout the parenchyma (**Fig. 4A**). By contrast, IPF

311   matrix scaffolds had pervasive dense fibroconnective structures, with abnormal disorganized

312   architecture, honeycombing, and no apparent airways or vessels. Scanning electron microscopy

313   revealed dramatic disruption of normal alveolar architecture in IPF scaffolds (**Fig. 4B**).

314   Topography of collagen fibers in IPF scaffolds was visualized by inverted color micrographs of

315   trichrome staining, which showed dense fibrous bundles in IPF scaffolds and stereotypical porous

316   (alveolar-like) networks in normal lung scaffolds (**Fig. 4C**). Transmission electron microscopy

317   showed dense fibrous bands (F) of extracellular matrix in IPF matrix scaffolds with minimal

318   evidence of normal basement membrane, whereas normal lung matrix scaffolds had abundant

319   airspaces (A), delicate basement membrane (arrow), and alveolar capillaries (C; **Fig. 4D**).

320   Uniaxial mechanical testing of IPF and normal tissues and scaffolds indicated that IPF tissues

321   and scaffolds were approximately 20× stiffer at 5% strain and approximately 5× stiffer at 20%

322   strain compared to normal tissues and scaffolds (**Fig. 4E**). Importantly, mechanical testing also

323   confirmed that the processing of native tissues to obtain matrix scaffolds did not alter the

324   mechanical properties of matrix scaffolds from native tissues, as differences in elastic modulus

325   between native tissues and matrix scaffolds were not significant (**Fig. 4F,G**).

326

327   **IPF matrix scaffolds support disease-like phenotype of lung fibroblasts.** Normal human lung

328   fibroblasts were added to IPF and normal lung matrix scaffolds and cultured *in vitro* for 7 days.

329   H&E staining showed that the phenotype of normal human lung fibroblasts varied between cells

330   cultured in IPF and normal lung matrix scaffolds (**Fig. 5A**). Fibroblasts in IPF matrix scaffolds

331   showed higher expression of alpha smooth muscle actin than fibroblasts in normal lung matrix

332   scaffolds. Morphologic similarities between fibroblasts cultured in IPF scaffolds and IPF native

333   tissue were observed (**Fig. 5B**). In contrast, immunostaining of FOXO3, a transcription factor

334   whose downregulation is linked to fibrogenesis[34], showed lower expression in human lung

14

Figure 4 | Structural, topographical, and mechanical characterizations of IPF lung scaffolds. Representative images of IPF and normal lung scaffolds: (**A**) gross photography, (**B**) scanning electron microscopy, (**C**) light microscopy (inverted color micrograph) of trichome staining demonstrating topography of ECM fibers in IPF scaffolds, (**D**) transmission electron microscopy. A: airspace, C: alveolar capillary, E: elastin bundle fragments, F: fibroconnective collagenous matrix, arrow: basement membrane. (**E**) Representative uniaxial stress-strain curves of IPF and normal lung tissues and matrix scaffolds. (**F**) Change in uniaxial mechanical stress from normal lung tissues and matrix scaffolds. (**G**) Tangent modulus values. Statistical analyses between tissues and scaffolds were performed using Student's t-test, with significance when $p < 0.05$. All values represent mean ± standard deviation.

335   fibroblasts cultured on IPF matrix scaffolds compared to fibroblasts cultured on normal lung matrix

336   scaffolds (**Fig. 5C**). Consistent with alpha smooth muscle immunohistochemical staining, gene

337   expression analysis showed significant upregulation of ACTA2 (alpha smooth muscle actin).

338   Additional upregulated fibrosis-specific markers of fibroblast activation included COL1A1

339   (collagen type I, subunit α1), MMP2, PDGFC, PTEN, and PRRX1 (**Fig. 5D**). Activation of

340   fibroblasts *in vitro* was also assessed by quantification of secreted basic fibroblast growth factor

341   (bFGF) and transforming growth factor beta (TGFβ), with normal human lung fibroblasts cultured

342   on tissue culture plastic as a standard control. Interestingly, secretion of bFGF and TGFβ were

343   both highest with fibroblasts cultured in IPF matrix scaffolds (**Fig. 5E,F**). Notably, secreted TGFβ

344   was significantly higher in IPF matrix scaffolds compared to normal lung matrix scaffolds,

345   suggesting that substrate stiffness may have influenced secretion of TGFβ.

346

347   **IPF matrix scaffolds provide a disease-specific environment for testing antifibrotic agents.**

348   Pulmonary fibroblasts in IPF matrix scaffolds showed a mean growth rate (linear fit: slope = 6.74,

349   R^2 = 0.98) over 80% faster than fibroblasts in normal lung matrix scaffolds (linear fit: slope = 3.70,

350   R^2 = 0.93; **Fig. 6A**, no drug), consistent with the fibroproliferative process characteristic of human

351   IPF. To assess differences in phenotype between fibroblasts cultured on IPF matrix scaffolds and

352   the conventional drug testing substrate tissue culture plastic, disease-associated gene expression

353   and growth factor secretion were analyzed. Fibroblasts cultured in IPF matrix scaffolds expressed

354   significantly higher COL1A1 and MMP2 than fibroblasts cultured on plastic (**Fig. 6B**), and

355   secreted more profibrotic growth factors bFGF and TGFβ than fibroblasts cultured in normal lung

356   matrix or on plastic (**Fig. 6C,D**), suggesting that the presence of disease-specific matrix resulted

357   in more disease-associated fibroblast phenotype *in vitro* compared to fibroblasts on plastic. When

358   exposed to antifibrotic agent PF3644022, a potent ATP-competitive MK2 inhibitor, pulmonary

359   fibroblasts cultured in IPF matrix scaffolds demonstrated significant reduction in cell number

360   compared to untreated fibroblasts over 6 days. PF3644022 also reduced expression of key IPF-
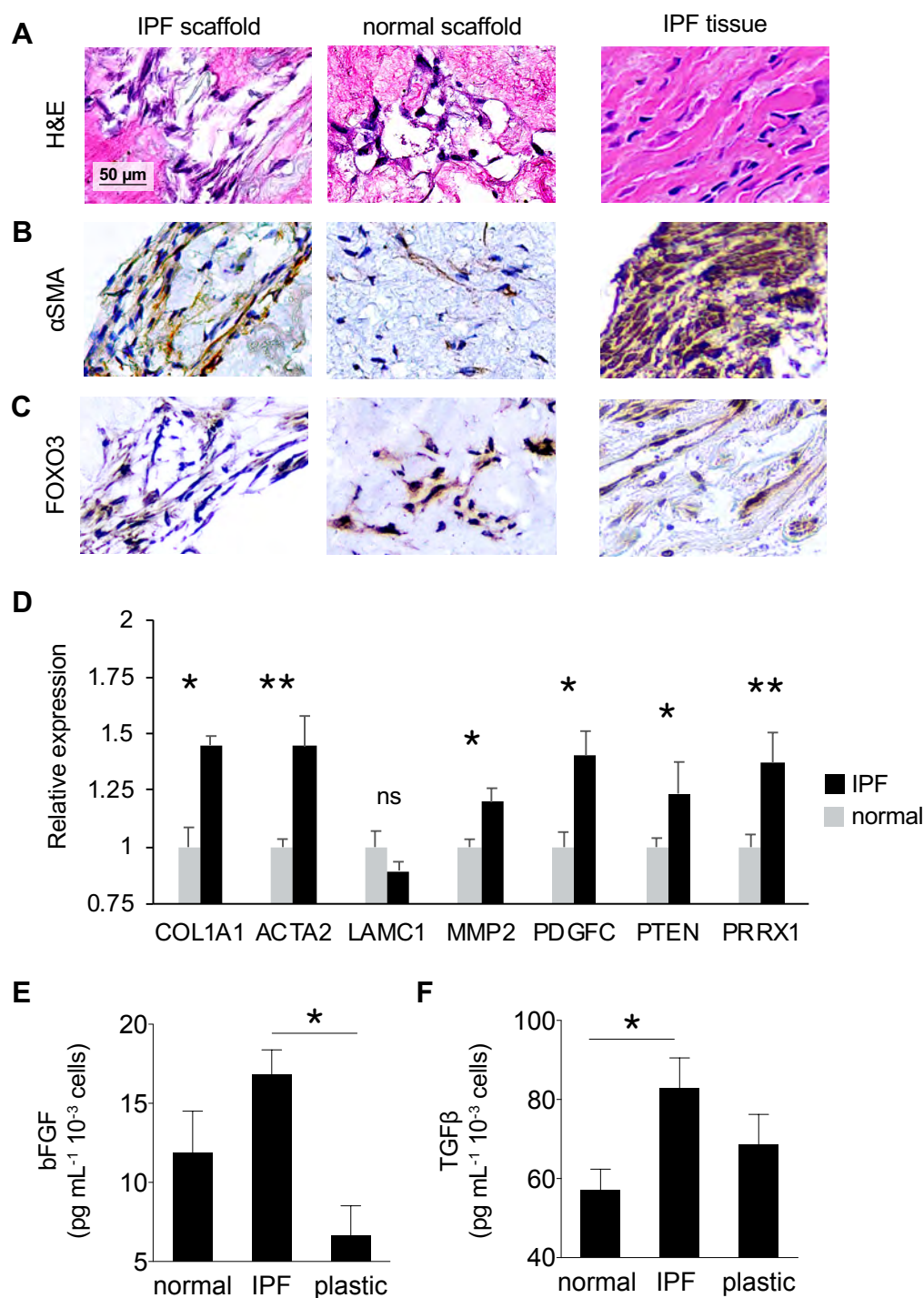
15

Figure 5 | Phenotype of lung fibroblasts in IPF and normal lung scaffolds. Representative micrographs of (**A**) H&E and immunohistochemical staining of (**B**) alpha smooth muscle actin (αSMA) and (**C**) Forkhead box O3 (FOXO3). (**D**) Gene expression of normal human lung fibroblasts cultured in IPF and normal lung scaffolds. * $p < 0.05$, ** $p < 0.01$, ns: not significant. Quantification by ELISA of (**E**) basic fibroblast growth factor (bFGF, * $p < 0.05$) and (**F**) transforming growth factor beta (TGFβ, * $p < 0.05$) secreted by normal human lung fibroblast cultured in IPF and normal lung scaffolds and on tissue culture plastic. All values represent mean ± standard deviation.
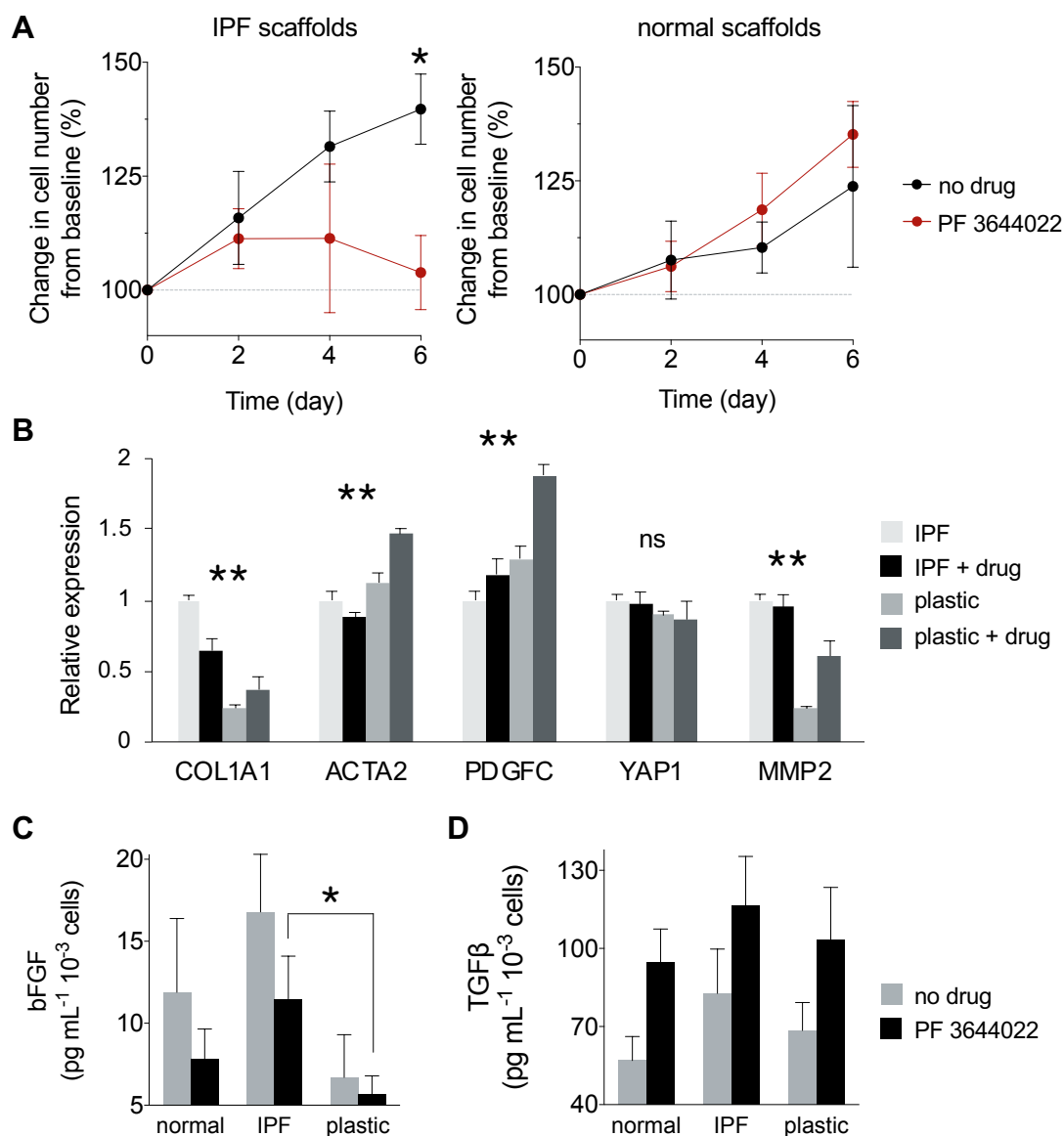
Figure 6 | Demonstration of anti-fibrotic drug testing in IPF lung scaffolds. (**A**) Growth curves of normal human lung fibroblasts over 6 days of treatment with PF 3644022. (**B**) Gene expression of normal human lung fibroblasts cultured on IPF scaffolds and tissue culture plastic. * $p < 0.05$, ** $p < 0.01$. Quantification by ELISA of (**C**) basic fibroblast growth factor (bFGF, $p = 0.0024$ by ANOVA) and (**D**) transforming growth factor beta (TGFβ, $p = 0.0084$ by ANOVA) secreted by normal lung fibroblast cultured in IPF and normal lung scaffolds and on tissue culture plastic. All values represent mean ± standard deviation.

361   associated genes COL1A1 and ACTA2 by fibroblasts in IPF matrix scaffolds (**Fig. 6B**) – an

362   expected result not observed in fibroblasts cultured on plastic. Similarly, PF3644022 reduced

363   secretion of bFGF by fibroblasts cultured in IPF matrix scaffolds (**Fig. 6C**). Interestingly, secretion

364   of TGFβ by fibroblasts exposed to PF3644022 trended upward across all substrates (**Fig. 6D**).

365   Altogether, these results confirm the activation and diseased phenotype of pulmonary fibroblasts

366   cultured in IPF matrix, and demonstrate the feasibility of testing antifibrotic agents in an *in-vitro*

367   substrate environment with IPF disease-specific features not otherwise present in tissue culture

368   plastic or other conventional drug screening platforms.

369

370   **DISCUSSION**

371

372   Using a physiomimetic approach, we developed an IPF disease-specific 3D cell culture substrate

373   comprised of fibrotic human lung extracellular matrix. Through biomolecular and physico-

374   mechanical characterizations, we show that this disease-specific substrate has numerous

375   physical and compositional features of the human IPF diseased extracellular matrix environment.

376   We also demonstrate the applicability of this substrate for pharmaceutical drug testing. As the

377   critical need for effective IPF drugs persists, human IPF disease-specific cell culture substrates

378   could enable more predictive disease models and drug screening platforms, and accelerate

379   development of new drugs for the treatment of IPF.

380

381   Human IPF is a chronic, aging-related disease of unknown etiology typically diagnosed at an

382   advanced stage, and is therefore challenging to model. Both animal[10,13] and *in-vitro* models[18,19,35-

383   37] have been used to gain insights into the cellular and molecular mechanisms of IPF. Although

384   animal models of IPF have been developed in mice, rats, hamsters, guinea pigs, rabbits, cats,

385   dogs, sheep, donkeys, horses, and non-human primates,[11,38-40] no animal model fully

386   recapitulates the pathophysiology of human IPF – specifically, the histologic pattern of usual

16

387   interstitial pneumonia and progressive fibrotic disease.[13] Furthermore, while animal models may

388   inform various aspects of fibrotic lung disease, significant anatomical, biological, and

389   immunological differences from humans reduce pathophysiological relevance to human IPF.

390   Notably, the American Thoracic Society has emphasized the importance of developing

391   'humanized' models of IPF to increase relevance of animal models of IPF to the human disease.[41]

392

393   Because animal models of IPF are inherently limited, *in-vitro* models are an indispensable tool in

394   basic and translational studies of human IPF. Previous studies have implicated multiple cellular

395   processes in pulmonary fibrosis including epithelial cell apoptosis[42], epithelial–mesenchymal

396   transition[43], and differentiation of fibroblasts to myofibroblasts[44] that result in significant

397   remodeling and deposition of fibrotic ECM. Conventional two-dimensional (2D) models of IPF

398   typically utilize monolayers of pulmonary myofibroblasts, the primary effector cells of IPF[45], on

399   tissue culture plastic, enabling mechanistic studies in controlled experimental settings. However,

400   cells cultured in 2D models experience artificial, non-physiological conditions that categorically

401   lack the appropriate three-dimensional (3D) spatial gradients – chemical, mechanical,

402   topographical – in which all lung cells naturally reside within the body. Constrained to one spatial

403   plane, cells in 2D models are immobilized, experience limited cell–cell interactions, and display

404   inhibited cytokinesis and chemotaxis, artificial flattened morphology, unnatural apical-basal

405   polarization, and abnormal integrin and cell-surface receptor expression and distribution.[46-48]

406   Furthermore, tissue culture plastic has non-physiological topography and stiffness (> 1,000

407   kPa)[49], which has been shown to drive atypical cytoskeletal rearrangements[50], perturb

408   homeostatic gene expression[51], and induce epigenetic modifications of fibroblasts[52].

409

410   Pulmonary fibroblasts cultured in 3D models, however, adhere to substrates at multiple focal

411   adhesion points[53], and experience more *in vivo*-like stress–strain[47] and soluble[54] gradients. Lung

412   fibroblasts cultured in hydrogels of collagen type I, a structural ECM component upregulated in

17

413   IPF, previously displayed contraction of collagen hydrogels, whose resistance to cell-generated

414   forces was proportional to expression of αSMA by fibroblasts.[55] Notably, collagen type I hydrogels

415   are comprised of a single structural ECM component, and thus lack the complex signaling and

416   regulation of the multi-component ECM in the fibrotic disease environment. As paracrine, cell–

417   cell, and cell–matrix interactions are known to drive progression of fibrotic lung disease,[56] disease-

418   specific 3D cell culture substrates are critical for improving *in-vitro* models of IPF, and should

419   ideally recapitulate the structure, mechanics, and biochemical composition of diseased human

420   lung tissue.

421

422   In this study, biochemical and mass spectrometry analyses confirmed that IPF matrix scaffolds

423   had: (*i*) increased collagens and decreased elastin consistent with increased stiffness and

424   decreased compliance, (*ii*) increased proteoglycans, whose covalently bound glycosaminoglycan

425   side chains chondroitin sulfate, dermatan sulfate, heparan sulfate, and hyaluronic acid have been

426   shown to be structurally altered and increased in IPF lungs[57], and (*iii*) abnormal profile of

427   glycoproteins. Proteoglycans influence viscoelastic properties, cell differentiation, and tissue

428   morphogenesis, and in particular heparan sulfate coordinates ligand–receptor binding of FGF,

429   PDGF, TGFβ, and VEGF[58] – growth factors involved in pathologic tissue remodeling and detected

430   in IPF matrix scaffolds. Biglycan, a small leucine-rich proteoglycan (SLRP) known to be altered in

431   fibrosis and correlated with lung mechanics through influence on ECM assembly[59], was increased

432   over 600% in IPF matrix scaffolds. The perturbed profile of glycoproteins in IPF matrix scaffolds

433   included: increased fibrillin 2, a collagenase-resistant glycoprotein that is associated with the 10-

434   nm microfibrils of the basal lamina and regulates the bioavailability of TGBβ through latent

435   transforming growth factor β binding proteins (LTBP)[60], and increased periostin, a matricellular

436   glycoprotein that promotes fibroblast proliferation, localization of fibrogenic growth factors,

437   collagen type I production, and collagen crosslinking[61]. Notably, the loss of basement membrane

438   components including collagen type IV[29], laminin, and nidogen in IPF tissues and matrix scaffolds

18

439   suggests that the use of basement membrane extracts such as Matrigel in models of IPF has

440   minimal pathophysiologic relevance.

441

442   The stiffness of fibrotic lung tissue (60 ± 40 kPa) is significantly higher than the stiffness of normal

443   lung tissue (7 ± 6 kPa)[35,49], which has critical implications for the stiffness of cell culture substrates

444   in models of IPF, especially for *in-vitro* culture of pulmonary fibroblasts, which exhibit complex

445   mechanotransduction[20,62] and have 'mechanical memory'[63]. In this study, fibrotic human lung

446   ECM scaffolds recapitulated the mechanical differences between normal and fibrotic lung tissues

447   (**Fig. 4**), and supported increased secretion of bFGF and TGFβ by normal human lung fibroblasts

448   (**Fig. 5E,F**), suggesting that the IPF matrix scaffolds have disease-specific mechanics and

449   regulatory signals relevant to human IPF. Notably, pulmonary fibroblasts cultured in fibrotic lung

450   ECM previously confirmed the regulatory role of ECM in the activation of myofibroblasts *in vitro*[36],

451   and demonstrated significant effects of substrate stiffness on fibroblast activation and

452   differentiation into myofibroblasts. Myofibroblast differentiation has also been shown to be driven

453   by increased ECM stiffness through mechanisms independent of TGFβ[20]. Interestingly, previous

454   studies wherein normal and IPF fibroblasts were cultured across ECM from normal and IPF lungs

455   revealed that IPF ECM had a greater influence on fibroblast gene expression than cell origin[64],

456   further indicating the central role of ECM in regulating disease-associated gene expression.

457   Altogether, these results highlight the critical importance of providing disease-specific signals from

458   the ECM environment in models of fibrotic lung disease.

459

460   In spite of decades of basic and translational research, the persisting struggle to successfully

461   translate promising preclinical drug candidates to drugs approved to treat IPF highlights the

462   limited effectiveness of disease models used in IPF drug discovery, which is likely attributable to

463   the failure of IPF models to recapitulate key pathophysiological features of the human disease.

464   Early-stage drug discovery assays are typically conducted on tissue culture plastic (e.g.,

19

465   polystyrene) with or without collagen type I coating, and supplemental TGFβ (e.g., 1 – 5 ng mL^{-1})

466   to activate primary or immortalized human lung fibroblasts – an entrenched *in-vitro* system that

467   has minimal pathophysiological relevance to the human IPF disease setting. With significant

468   financial costs and scientific, medical, and regulatory challenges associated with conducting

469   clinical trials in patients with IPF, preclinical assessments of antifibrotic compounds must be

470   sufficiently robust to inform go/no go decision making and yield reliably predictive data in order to

471   maximize the likelihood of advancing promising drug candidates to clinical trials.

472

473   In this study, we demonstrated the use of IPF disease-specific ECM in a 3D cell-based assay of

474   antifibrotic agent PF3644022 (an MK2 inhibitor in IPF model)[65]. As expected, fibroblasts cultured

475   on fibrotic lung ECM scaffolds and treated with PF3644022 exhibited greater sensitivity and drug

476   response, significantly different gene expression, and downregulation of genes associated with

477   ECM production compared to cells cultured on tissue culture plastic. We envision that disease-

478   specific ECM may be applicable across multiple stages of the drug discovery pipeline, from target

479   selection and hit identification through lead identification and optimization. The use of disease-

480   specific ECM substrates is consistent with the set of principles[66] defined for 'disease-relevant

481   assays' that specifically recommend ensuring: (*i*) substrate tension and mechanical forces are

482   appropriate, and (*ii*) extracellular matrix composition is relevant, with appropriate tissue

483   architecture, cell differentiation and function to enhance clinical translation of the *in-vitro* assay.

484   Ultimately, implementation of disease-specific ECM components or substrates into preclinical

485   human disease models and cell-based screening assays could increase clinical relevance and

486   success rates.

487

488   There are several limitations to the present study: (*1*) This study investigated a small number of

489   human lungs (n = 6 total, n = 3 per group). Although this study was conducted with the minimum

490   number of human lungs required to achieve statistical significance between groups, investigation

491   of larger numbers of IPF lungs would offer opportunities for deeper statistical analyses and

492   potential correlations between matrix characteristics and disease phenotypes. (*2*) As IPF lung

493   specimens were procured from explanted tissues following lung transplantation, this study only

494   investigated fibrotic lung matrix from end-stage disease. While diagnosis of IPF remains a

495   significant clinical challenge, procurement of fibrotic human lung ECM at earlier stages of fibrotic

496   disease may not be feasible. (*3*) Human donor tissues present intrinsic biological variability that

497   could confound experimental results. To minimize variability between donors, acceptance criteria

498   for lungs were tightly defined and strictly implemented. Furthermore, as IPF is a disease with

499   demonstrable spatiotemporal heterogeneity, extensive histopathologic review was conducted by

500   a lung transplant pathologist to ensure only tissues and scaffolds with fibrosis scores ≥ 2 were

501   utilized. (*4*) Only one antifibrotic drug was evaluated in this study. Future studies will investigate

502   additional compounds to provide further evidence of the utility and benefits of IPF disease-specific

503   ECM substrates.

504

505   The IPF matrix scaffolds developed in this study may be useful for cell-based assays, but may

506   have limited applicability to high throughput drug screening systems, which typically utilize rapid

507   optical readouts in 96- and 384-well plate formats. Therefore, an alternative format of fibrotic lung

508   matrix, e.g., hydrogel, may be more suitable for high throughput applications. Future studies will

509   explore the development of additional IPF disease-specific ECM formats to address broader

510   research and development applications such as 'IPF-on-chip'. As IPF disease progression is

511   driven by a combination of lung and immune cell–cell and cell–matrix interactions, future studies

512   will also investigate co-cultures with pulmonary macrophages, epithelial and smooth muscle cells,

513   and the effects of IPF-associated growth factors on lung cells *in vitro*. Altogether, an *in-vitro* model

514   with a disease-specific substrate of human IPF disease environment can help elucidate

515   underlying idiopathologies of IPF, enable development of effective IPF therapeutics, and may

516   serve as a template approach for the development of fibrosis-specific cell culture substrates in

517   other human organs and tissues susceptible to fibrotic disease.

518

519   **CONCLUSIONS**

520   We developed a pulmonary fibrosis-specific cell culture substrate comprised of intact fibrotic lung

521   extracellular matrix that recapitulated *in vitro* key features of the human IPF disease environment

522   and supported the disease-associated phenotype of human lung fibroblasts. We also

523   demonstrated feasibility of testing antifibrotic agents using this substrate, which may be applicable

524   in cell-based assays in early-stage drug discovery.

525

526   **ACKNOWLEDGEMENTS**

534

535   **AUTHOR CONTRIBUTIONS**

536   I.G., E.A., and J.D.O. designed the study. I.G., E.A., J. X., N. K., A. N., and E.G. performed

537   experiments. I.G., E.A., and J.D.O. co-analyzed data, co-wrote the manuscript.

22

538 **REFERENCES**

539

540 1 Lederer, D. J. & Martinez, F. J. Idiopathic Pulmonary Fibrosis. *N Engl J Med* **378**, 1811-

541 1823, doi:10.1056/NEJMra1705751 (2018).

542 2 Coward, W. R., Saini, G. & Jenkins, G. The pathogenesis of idiopathic pulmonary fibrosis.

543 *Ther Adv Respir Dis* **4**, 367-388, doi:10.1177/1753465810379801 (2010).

544 3 Noble, P. W., Barkauskas, C. E. & Jiang, D. Pulmonary fibrosis: patterns and perpetrators.

545 *J Clin Invest* **122**, 2756-2762, doi:10.1172/JCI60323 (2012).

546 4 Sauleda, J., Nunez, B., Sala, E. & Soriano, J. B. Idiopathic Pulmonary Fibrosis:

547 Epidemiology, Natural History, Phenotypes. *Med Sci (Basel)* **6**,

548 doi:10.3390/medsci6040110 (2018).

549 5 Ley, B. & Collard, H. R. Epidemiology of idiopathic pulmonary fibrosis. *Clin Epidemiol* **5**,

550 483-492, doi:10.2147/CLEP.S54815 (2013).

551 6 Hutchinson, J., Fogarty, A., Hubbard, R. & McKeever, T. Global incidence and mortality of

552 idiopathic pulmonary fibrosis: a systematic review. *Eur Respir J* **46**, 795-806,

553 doi:10.1183/09031936.00185114 (2015).

554 7 Vancheri, C., Failla, M., Crimi, N. & Raghu, G. Idiopathic pulmonary fibrosis: a disease with

555 similarities and links to cancer biology. *Eur Respir J* **35**, 496-504,

556 doi:10.1183/09031936.00077309 (2010).

557 8 Ryu, J. H. *et al.* Idiopathic pulmonary fibrosis: evolving concepts. *Mayo Clin Proc* **89**, 1130-

558 1142, doi:10.1016/j.mayocp.2014.03.016 (2014).

559 9 Plantier, L. *et al.* Physiology of the lung in idiopathic pulmonary fibrosis. *Eur Respir Rev* **27**,

560 doi:10.1183/16000617.0062-2017 (2018).

561 10 Moore, B. B. & Hogaboam, C. M. Murine models of pulmonary fibrosis. *Am J Physiol Lung*

562 *Cell Mol Physiol* **294**, L152-160, doi:10.1152/ajplung.00313.2007 (2008).

563   11   Mouratis, M. A. & Aidinis, V. Modeling pulmonary fibrosis with bleomycin. *Curr Opin Pulm*

564   *Med* **17**, 355-361, doi:10.1097/MCP.0b013e328349ac2b (2011).

565   12   Antje Moeller, J. C. R.-L., Lingqiao Wang, Jack Gauldie, Martin Kolb. Models of pulmonary

566   fibrosis. *Drug Discovery Today Disease Models* **3**, 243-249 (2006).

567   13   B, B. M. *et al.* Animal models of fibrotic lung disease. *Am J Respir Cell Mol Biol* **49**, 167-

568   179, doi:10.1165/rcmb.2013-0094TR (2013).

569   14   Nichols, J. E., Niles, J. A., Vega, S. P. & Cortiella, J. Novel in vitro respiratory models to

570   study lung development, physiology, pathology and toxicology. *Stem Cell Res Ther* **4**

571   **Suppl 1**, S7, doi:10.1186/scrt368 (2013).

572   15   Zhou, Y. *et al.* Extracellular matrix in lung development, homeostasis and disease. *Matrix*

573   *Biol* **73**, 77-104, doi:10.1016/j.matbio.2018.03.005 (2018).

574   16   Shimbori, C., Gauldie, J. & Kolb, M. Extracellular matrix microenvironment contributes

575   actively to pulmonary fibrosis. *Curr Opin Pulm Med* **19**, 446-452,

576   doi:10.1097/MCP.0b013e328363f4de (2013).

577   17   Kristensen, J. H. *et al.* The role of extracellular matrix quality in pulmonary fibrosis.

578   *Respiration* **88**, 487-499, doi:10.1159/000368163 (2014).

579   18   Hetzel, M., Bachem, M., Anders, D., Trischler, G. & Faehling, M. Different effects of growth

580   factors on proliferation and matrix production of normal and fibrotic human lung fibroblasts.

581   *Lung* **183**, 225-237, doi:10.1007/s00408-004-2534-z (2005).

582   19   Correll, K. A. *et al.* TGF beta inhibits HGF, FGF7, and FGF10 expression in normal and IPF

583   lung fibroblasts. *Physiol Rep* **6**, e13794, doi:10.14814/phy2.13794 (2018).

584   20   Huang, X. *et al.* Matrix stiffness-induced myofibroblast differentiation is mediated by

585   intrinsic mechanotransduction. *Am J Respir Cell Mol Biol* **47**, 340-348,

586   doi:10.1165/rcmb.2012-0050OC (2012).

24

587   21   Wight, T. N. & Potter-Perigo, S. The extracellular matrix: an active or passive player in

588   fibrosis? *Am J Physiol Gastrointest Liver Physiol* **301**, G950-955,

589   doi:10.1152/ajpgi.00132.2011 (2011).

590   22   Lehtonen, S. T. *et al.* Pirfenidone and nintedanib modulate properties of fibroblasts and

591   myofibroblasts in idiopathic pulmonary fibrosis. *Respir Res* **17**, 14, doi:10.1186/s12931-

592   016-0328-5 (2016).

593   23   O'Neill, J. D. *et al.* Decellularization of human and porcine lung tissues for pulmonary tissue

594   engineering. *Ann Thorac Surg* **96**, 1046-1055; discussion 1055-1046,

595   doi:10.1016/j.athoracsur.2013.04.022 (2013).

596   24   Wagner, D. E. *et al.* Three-dimensional scaffolds of acellular human and porcine lungs for

597   high throughput studies of lung disease and regeneration. *Biomaterials* **35**, 2664-2679,

598   doi:10.1016/j.biomaterials.2013.11.078 (2014).

599   25   Balestrini, J. L. *et al.* Comparative biology of decellularized lung matrix: Implications of

600   species mismatch in regenerative medicine. *Biomaterials* **102**, 220-230,

601   doi:10.1016/j.biomaterials.2016.06.025 (2016).

602   26   Gilpin, S. E. & Wagner, D. E. Acellular human lung scaffolds to model lung disease and

603   tissue regeneration. *Eur Respir Rev* **27**, doi:10.1183/16000617.0021-2018 (2018).

604   27   Ashcroft, T., Simpson, J. M. & Timbrell, V. Simple method of estimating severity of

605   pulmonary fibrosis on a numerical scale. *J Clin Pathol* **41**, 467-470,

606   doi:10.1136/jcp.41.4.467 (1988).

607   28   Lu, J., Auduong, L., White, E. S. & Yue, X. Up-regulation of heparan sulfate 6-O-sulfation in

608   idiopathic pulmonary fibrosis. *Am J Respir Cell Mol Biol* **50**, 106-114,

609   doi:10.1165/rcmb.2013-0204OC (2014).

610   29   Sand, J. M. *et al.* MMP mediated degradation of type IV collagen alpha 1 and alpha 3

611   chains reflects basement membrane remodeling in experimental and clinical fibrosis--

612   validation of two novel biomarker assays. *PLoS One* **8**, e84934,

613   doi:10.1371/journal.pone.0084934 (2013).

614 30 S. Ohshimo, K. H., F. Bonella, C. Yamaoka, Y. Horimasu, H. Iwamoto, N. Ishikawa, K.

615   Fujitaka, H. Murai, H. Hamada, N. Hattori, N. Hirohashi, K. Tanigawa, J. Guzman, U.

616   Costabel, N. Kohno. Growth Differentiation Factor-15 (gdf-15) As Prognostic Factor For

617   Idiopathic Pulmonary Fibrosis. *Am J Respir Crit Care Med* **191** (2015).

618 31 Ruan, W. & Ying, K. Abnormal expression of IGF-binding proteins, an initiating event in

619   idiopathic pulmonary fibrosis? *Pathol Res Pract* **206**, 537-543,

620   doi:10.1016/j.prp.2010.03.010 (2010).

621 32 Pilewski, J. M., Liu, L., Henry, A. C., Knauer, A. V. & Feghali-Bostwick, C. A. Insulin-like

622   growth factor binding proteins 3 and 5 are overexpressed in idiopathic pulmonary fibrosis

623   and contribute to extracellular matrix deposition. *Am J Pathol* **166**, 399-407,

624   doi:10.1016/S0002-9440(10)62263-8 (2005).

625 33 Avcuoglu, S. *et al.* Neurotrophic tyrosine kinase receptor B/neurotrophin 4 signaling axis is

626   perturbed in clinical and experimental pulmonary fibrosis. *Am J Respir Cell Mol Biol* **45**,

627   768-780, doi:10.1165/rcmb.2010-0195OC (2011).

628 34 Al-Tamari, H. M. *et al.* FoxO3 an important player in fibrogenesis and therapeutic target for

629   idiopathic pulmonary fibrosis. *EMBO Mol Med* **10**, 276-293,

630   doi:10.15252/emmm.201606261 (2018).

631 35 Hinz, B. Mechanical aspects of lung fibrosis: a spotlight on the myofibroblast. *Proc Am*

632   *Thorac Soc* **9**, 137-147, doi:10.1513/pats.201202-017AW (2012).

633 36 Booth, A. J. *et al.* Acellular normal and fibrotic human lung matrices as a culture system for

634   in vitro investigation. *Am J Respir Crit Care Med* **186**, 866-876, doi:10.1164/rccm.201204-

635   0754OC (2012).

636   37   Thannickal, V. J. *et al.* Matrix biology of idiopathic pulmonary fibrosis: a workshop report of

637   the national heart, lung, and blood institute. *Am J Pathol* **184**, 1643-1651,

638   doi:10.1016/j.ajpath.2014.02.003 (2014).

639   38   Tashiro, J. *et al.* Exploring Animal Models That Resemble Idiopathic Pulmonary Fibrosis.

640   *Front Med (Lausanne)* **4**, 118, doi:10.3389/fmed.2017.00118 (2017).

641   39   Paul F. Mercer, K. A.-B., Ian M. Adcock, Richard G. Knowles. Translational models of lung

642   disease. *Clinical Science* **128** 235-256, doi:10.1042/CS20140373 (2015).

643   40   Organ, L. *et al.* A novel segmental challenge model for bleomycin-induced pulmonary

644   fibrosis in sheep. *Exp Lung Res* **41**, 115-134, doi:10.3109/01902148.2014.985806 (2015).

645   41   R. Gisli Jenkins, B. B. M., Rachel C. Chambers, Oliver Eickelberg, Melanie Konigshoff,

646   Martin Kolb, Geoffrey J. Laurent, Carmel B. Nanthakumar, Mitchell A. Olman, Annie Pardo,

647   Moises Selman, Dean Sheppard, Patricia J. Sime, Andrew M. Tager, Amanda L. Tatler,

648   Victor J. Thannickal, and Eric S. White; on behalf of the ATS Assembly on Respiratory Cell

649   and Molecular Biology. An Official American Thoracic Society Workshop Report: Use of

650   Animal Models for the Preclinical Assessment of Potential Therapies for Pulmonary

651   Fibrosis. *Am J Respir Cell Mol Biol* **56**, 667-679, doi:10.1165/rcmb.2017-0096ST (2017).

652   42   Lepparanta, O. *et al.* Regulation of TGF-beta storage and activation in the human idiopathic

653   pulmonary fibrosis lung. *Cell Tissue Res* **348**, 491-503, doi:10.1007/s00441-012-1385-9

654   (2012).

655   43   Kim, K. K. *et al.* Alveolar epithelial cell mesenchymal transition develops in vivo during

656   pulmonary fibrosis and is regulated by the extracellular matrix. *Proc Natl Acad Sci U S A*

657   **103**, 13180-13185, doi:10.1073/pnas.0605669103 (2006).

658   44   Kis, K., Liu, X. & Hagood, J. S. Myofibroblast differentiation and survival in fibrotic disease.

659   *Expert Rev Mol Med* **13**, e27, doi:10.1017/S1462399411001967 (2011).

660   45   Todd, N. W., Luzina, I. G. & Atamas, S. P. Molecular and cellular mechanisms of

661   pulmonary fibrosis. *Fibrogenesis Tissue Repair* **5**, 11, doi:10.1186/1755-1536-5-11 (2012).

662 46 Sundarakrishnan, A., Chen, Y., Black, L. D., Aldridge, B. B. & Kaplan, D. L. Engineered cell

663   and tissue models of pulmonary fibrosis. *Adv Drug Deliv Rev* **129**, 78-94,

664   doi:10.1016/j.addr.2017.12.013 (2018).

665 47 Baker, B. M. & Chen, C. S. Deconstructing the third dimension: how 3D culture

666   microenvironments alter cellular cues. *J Cell Sci* **125**, 3015-3024, doi:10.1242/jcs.079509

667   (2012).

668 48 Griffith, L. G. & Swartz, M. A. Capturing complex 3D tissue physiology in vitro. *Nat Rev Mol*

669   *Cell Biol* **7**, 211-224, doi:10.1038/nrm1858 (2006).

670 49 Skardal, A., Mack, D., Atala, A. & Soker, S. Substrate elasticity controls cell proliferation,

671   surface marker expression and motile phenotype in amniotic fluid-derived stem cells. *J*

672   *Mech Behav Biomed Mater* **17**, 307-316, doi:10.1016/j.jmbbm.2012.10.001 (2013).

673 50 Doyle, A. D. & Yamada, K. M. Mechanosensing via cell-matrix adhesions in 3D

674   microenvironments. *Exp Cell Res* **343**, 60-66, doi:10.1016/j.yexcr.2015.10.033 (2016).

675 51 Raab, M., Shin, J. W. & Discher, D. E. Matrix elasticity in vitro controls muscle stem cell

676   fate in vivo. *Stem Cell Res Ther* **1**, 38, doi:10.1186/scrt38 (2010).

677 52 Nestor, C. E. *et al.* Rapid reprogramming of epigenetic and transcriptional profiles in

678   mammalian culture systems. *Genome Biol* **16**, 11, doi:10.1186/s13059-014-0576-y (2015).

679 53 Lou, J., Stowers, R., Nam, S., Xia, Y. & Chaudhuri, O. Stress relaxing hyaluronic acid-

680   collagen hydrogels promote cell spreading, fiber remodeling, and focal adhesion formation

681   in 3D cell culture. *Biomaterials* **154**, 213-222, doi:10.1016/j.biomaterials.2017.11.004

682   (2018).

683 54 Klingberg, F. *et al.* Prestress in the extracellular matrix sensitizes latent TGF-beta1 for

684   activation. *J Cell Biol* **207**, 283-297, doi:10.1083/jcb.201402006 (2014).

685 55 Arora, P. D., Narani, N. & McCulloch, C. A. The compliance of collagen gels regulates

686   transforming growth factor-beta induction of alpha-smooth muscle actin in fibroblasts. *Am J*

687   *Pathol* **154**, 871-882, doi:10.1016/s0002-9440(10)65334-5 (1999).

688   56   Barkauskas, C. E. & Noble, P. W. Cellular mechanisms of tissue fibrosis. 7. New insights

689   into the cellular mechanisms of pulmonary fibrosis. *Am J Physiol Cell Physiol* **306**, C987-

690   996, doi:10.1152/ajpcell.00321.2013 (2014).

691   57   Westergren-Thorsson, G. *et al.* Increased deposition of glycosaminoglycans and altered

692   structure of heparan sulfate in idiopathic pulmonary fibrosis. *Int J Biochem Cell Biol* **83**, 27-

693   38, doi:10.1016/j.biocel.2016.12.005 (2017).

694   58   Forsten-Williams, K., Chu, C. L., Fannon, M., Buczek-Thomas, J. A. & Nugent, M. A.

695   Control of growth factor networks by heparan sulfate proteoglycans. *Ann Biomed Eng* **36**,

696   2134-2148, doi:10.1007/s10439-008-9575-z (2008).

697   59   Faffe, D. S. & Zin, W. A. Lung parenchymal mechanics in health and disease. *Physiol Rev*

698   **89**, 759-775, doi:10.1152/physrev.00019.2007 (2009).

699   60   Davis, M. R. & Summers, K. M. Structure and function of the mammalian fibrillin gene

700   family: implications for human connective tissue diseases. *Mol Genet Metab* **107**, 635-647,

701   doi:10.1016/j.ymgme.2012.07.023 (2012).

702   61   O'Dwyer, D. N. & Moore, B. B. The role of periostin in lung fibrosis and airway remodeling.

703   *Cell Mol Life Sci* **74**, 4305-4314, doi:10.1007/s00018-017-2649-z (2017).

704   62   Branco da Cunha, C. *et al.* Influence of the stiffness of three-dimensional alginate/collagen-

705   I interpenetrating networks on fibroblast biology. *Biomaterials* **35**, 8927-8936,

706   doi:10.1016/j.biomaterials.2014.06.047 (2014).

707   63   Balestrini, J. L., Chaudhry, S., Sarrazy, V., Koehler, A. & Hinz, B. The mechanical memory

708   of lung myofibroblasts. *Integrative Biology* **4**, 410-421, doi:10.1039/c2ib00149g (2012).

709   64   Parker, M. W. *et al.* Fibrotic extracellular matrix activates a profibrotic positive feedback

710   loop. *J Clin Invest* **124**, 1622-1635, doi:10.1172/JCI71386 (2014).

711   65   Mourey, R. J. *et al.* A benzothiophene inhibitor of mitogen-activated protein kinase-

712   activated protein kinase 2 inhibits tumor necrosis factor alpha production and has oral anti-

713   inflammatory efficacy in acute and chronic models of inflammation. *J Pharmacol Exp Ther*

714   **333**, 797-807, doi:10.1124/jpet.110.166173 (2010).

715   66 Horvath, P. *et al.* Screening out irrelevant cell-based models of disease. *Nat Rev Drug*

716   *Discov* **15**, 751-769, doi:10.1038/nrd.2016.175 (2016).

717

718 **FIGURE CAPTIONS**

719

720 **Figure 1 | Overview of physiomimetic approach.** Our development of IPF disease-specific cell

721 culture substrates is guided by a physiomimetic approach that aims to identify and isolate the

722 human disease environment, then develop and investigate disease-specific ECM substrates *in*

723 *vitro* utilizing disease-relevant human cell types (e.g., pulmonary fibroblasts) whose phenotype

724 can be directly compared against diseased human IPF lung specimens prior to application in IPF

725 disease models and antifibrotic drug testing.

726

727 **Figure 2 | Histological & biochemical characterization of ECM structural components in**

728 **IPF lung tissues and matrix scaffolds.** Representative micrographs of histologic stains: (**A**)

729 hematoxylin and eosin (H&E), (**B**) trichrome (collagens, blue), and (**C**) Verhoeff–Van Gieson

730 (VVG, elastic fibers, black) demonstrating differences in histomorphology of IPF and normal lung

731 tissues and scaffolds. Star indicates representative region with severe fibrosis and loss of elastic

732 fibers. Quantification of structural ECM components (**D**) collagens and (**E**) elastin by biochemical

733 assays. (**F**) Changes from normal lung in structural ECM components in IPF. H&E: hematoxylin

734 and eosin, VVG: Verhoeff–Van Gieson.

735

736 **Figure 3 | Characterization of proteoglycans and glycoproteins in IPF lung tissues and**

737 **matrix scaffolds.** Representative micrographs of histologic stains: (**A**) Alcian blue

738 (proteoglycans, blue) and (**B**) pentachrome (acidic polysaccharides, green) demonstrating

739 differences in proteoglycans between IPF and normal lung tissues. Arrow indicates normal airway

740 epithelium. Quantification of sulfated glycosaminoglycan ECM components in (**C**) native tissues

741 and (**D**) matrix scaffolds. (**E**) Changes from normal lung in glycosaminoglycan ECM components

742 in IPF. Immunohistochemical staining of glycoprotein ECM components in IPF: (**F**) fibrillin 2, (**G**)

31

743   laminin γ1, (**H**) matrix gla protein (MGP), (**I**) periostin. (**J**) Quantification of glycoproteins by image

744   analysis of immunohistochemical staining using DensitoQuant software.

745

746   **Table 1 | Mass spectrometry analysis of IPF lung matrisome.** Changes from normal in

747   the abundance of IPF lung matrisome components. PG: proteoglycan, BM: basement membrane.

748

749   **Table 2 | Quantification of growth factors in IPF and normal lung matrix scaffolds.** Growth

750   factor concentrations were measured by multiplex growth factor array. Green arrow (▲) indicates

751   positive fold change (increase) from normal in concentration of growth factors. Red arrow (▼)

752   indicates negative fold change (decrease) from normal in concentration of growth factors. ND: not

753   detected.

754

755   **Figure 4 | Structural, topographical, and mechanical characterization of IPF**

756   **lung scaffolds.** Representative images of IPF and normal lung scaffolds: (**A**) gross photography,

757   (**B**) scanning electron microscopy, (**C**) light microscopy (inverted color micrograph) of trichome

758   staining demonstrating topography of ECM fibers in IPF scaffolds, (**D**) transmission electron

759   microscopy. A: airspace, C: alveolar capillary, E: elastin bundle fragments, F: fibroconnective

760   collagenous matrix, arrow: basement membrane. (**E**) Representative uniaxial stress-strain curves

761   of IPF and normal lung tissues and matrix scaffolds. (**F**) Change in uniaxial mechanical stress

762   from normal lung tissues and matrix scaffolds. (**G**) Tangent modulus values. Statistical analyses

763   between tissues and scaffolds were performed using Student's *t*-test, with significance when $p <$

764   0.05. All values represent mean ± standard deviation.

765

766   **Figure 5 | Phenotype of lung fibroblasts in IPF and normal lung scaffolds.** Representative

767   micrographs of (**A**) H&E and immunohistochemical staining of (**B**) alpha smooth muscle actin

768   (αSMA) and (**C**) Forkhead box O3 (FOXO3). (**D**) Gene expression of normal human lung

32

769   fibroblasts cultured in IPF and normal lung scaffolds. * $p <$ 0.05, ** $p <$ 0.01, ns:

770   not significant. Quantification by ELISA of (**E**) basic fibroblast growth factor (bFGF, * $p < 0.05$)

771   and (**F**) transforming growth factor beta (TGFβ, * $p < 0.05$) secreted by normal human lung

772   fibroblast cultured in IPF and normal lung scaffolds and on tissue culture plastic. All values

773   represent mean ± standard deviation.

774

775   **Figure 6 | Demonstration of antifibrotic drug testing in IPF lung scaffolds.** (**A**) Growth curves

776   of normal human lung fibroblasts over 6 days of treatment with PF3644022. (**B**) Gene expression

777   of normal human lung fibroblasts cultured on IPF scaffolds and tissue culture plastic. * $p < 0.05$,

778   ** $p < 0.01$. Quantification by ELISA of (**C**) basic fibroblast growth factor (bFGF, $p = 0.0024$ by

779   ANOVA) and (**D**) transforming growth factor beta (TGFβ, $p = 0.0084$ by ANOVA) secreted by

780   normal lung fibroblast cultured in IPF and normal lung scaffolds and on tissue culture plastic. All

781   values represent mean ± standard deviation.

782

783   **Supplementary Figure 1 | Characterization of human IPF and normal lung tissues.** (**A**)

784   Donor characteristics of IPF and normal lung tissues. (**B**) Representative chest radiographs of

785   IPF and normal lung donors. Arrows indicate changed lung shape, decreased lung volume,

786   and increased radiopacity consistent with pulmonary fibrosis. (**C**) Fibrosis scoring rubric used to

787   assess the extent of architectural disruption and fibrosis in human lung tissues. (**D**) Overview of

788   the description and quantity of tissue samples analyzed in this study. Samples were collected

789   from three regions (i.e., medial, lateral, peripheral) of right middle lobes. (**F**) Demonstration of

790   quantitative image analysis method used for fibrosis scoring. For each fibrosis score, a weighted

791   average is calculated from the ratios of the total area. Five high-power fields were analyzed per

792   region, and an average fibrosis score was calculated for each region. (**G**) Fibrosis scores of

793   all regions of IPF and normal lungs investigated in this study. Only regions of IPF lungs with

794   fibrosis score ≥ 2 (red triangle) were investigated in this study. * $p < 0.001$.

33

795 **Supplementary Figure 2 | Quality control assays of IPF and normal lung**

796 **matrix scaffolds.** Quantification of (**A**) DNA to confirm removal of nuclear material from IPF

797 and normal lung matrix scaffolds. (**B**) Results of sterility and mycoplasma assays. Prior to use in

798 studies, IPF and normal lung matrix scaffolds were tested for absence of bacteria and fungi.

799 Scaffolds were also tested for absence of mycoplasma using MycoAlert PLUS Mycoplasma

800 Detection Assay. * $p < 0.001$.

801

802 **Supplementary Table 1 | Antibodies and ELISA kits.**

803

804 **Supplementary Table 2 | Primers.**

805

806 **Supplementary Table 3 | Demographic and clinical characteristics of human lung donors.**

807 UIP, usual interstitial pneumonia.

808

809 **Supplementary Table 4 | Quantification of growth factors in IPF and normal lung tissues.**

810 Growth factor concentrations were measured by multiplex growth factor array. Green arrow (▲)

811 indicates positive fold change (increase) from normal in concentration of growth factors. Red

812 arrow (▼) indicates negative fold change (decrease) from normal in concentration of growth

813 factors. ND: not detected. * IPF-specific growth factor not detected in normal lung tissue.

34

814 **SUPPLEMENTARY INFORMATION**

815

816 **Characterization of human IPF and normal lung tissues.** Donor characteristics of IPF and

817 normal lung tissues were analyzed to confirm that there were no significant differences in age,

818 height, weight, body mass index, or smoking history (**Supplementary Fig. 1A, Supplementary**

819 **Table 3**). The mean lung allocation score for IPF donors was 55.0 ± 25.1, which was the only

820 significant difference between IPF and normal lung donors ($p < 0.05$). Chest radiographs of lung

821 donors confirmed absence of apparent injury or underlying disease in normal lungs, and enabled

822 assessment of the extent and distribution of pulmonary fibrosis in IPF lungs. In contrast to normal

823 lungs, which appeared radiolucent and aerated, IPF lungs displayed a morphologic pattern of

824 usual interstitial pneumonia consistent with IPF and marked by diffuse radiopacities, reticulation,

825 architectural distortion, and honeycombing, especially in peripheral and basal regions

826 (**Supplementary Fig. 1B**).

827

828 In order to characterize the histopathology of all tissues investigated, a fibrosis scoring rubric was

829 used to assess the extent of architectural disruption and fibrosis (**Supplementary Fig. 1C**).

830 Samples were systematically collected from the medial and lateral regions of the right middle and

831 right lower lobes. Histologic samples were evaluated by light microscopy, and fibrosis scores were

832 assigned and averaged across five high-power fields. All high-power fields were subjected to

833 imaging analyses to quantify the relative areas corresponding to each fibrosis score

834 (**Supplementary Fig. 1F**). To ensure to the maximum possible extent a consistent degree of

835 pulmonary fibrosis across all samples, only samples with average fibrosis score ≥ 2 (moderate or

836 severe fibrosis) were investigated in this study (**Supplementary Fig. 1G**).

837

838 **Mass spectrometry.** Protein profiling included short gel SDS-PAGE, in-gel digestion with trypsin,

839 and 2 hours LC-MS/MS. Samples were weighed and suspended in 130 μL of 2.0% modified RIPA

35

840   buffer with 1.6 mm stainless steel beads. Samples were homogenized in a Next Advance Bullet

841   Blender for 3 minutes at speed 10, then heated at 100°C for 30 minutes. Samples were then

842   sonicated and clarified by centrifugation. The protein concentration of the extract was determined

843   using Qubit fluorometry (Life Technologies). Each sample (10 µg) was processed by 2 cm SDS-

844   PAGE using a 10% Bis-Tris NuPAGE Novex mini gel (ThermoFisher) with the MES buffer system.

845   The mobility region was excised and processed by in-gel digestion with trypsin using a ProGest

846   robot (DigiLab) with the following protocol: (1) Wash with 25 mM ammonium bicarbonate followed

847   by acetonitrile. (2) Reduce with 10 mM dithiothreitol at 60°C followed by alkylation with 50 mM

848   iodoacetamide at room temperature. (3) Digest with sequencing grade trypsin (Promega) at 37°C

849   for 4 hours. (4) Quench with formic acid and analyzed without further processing.

850

851   Half of each digest was analyzed by nano LC-MS/MS with a Waters NanoAcquity HPLC system

852   interfaced to a mass spectrometer (Fusion Lumos, ThermoFisher). Peptides were loaded on a

853   trapping column and eluted over a 75 µm analytical column at 350 nL min^{-1} with a reverse phase

854   gradient for 2 hours. Both columns were packed with Luna C18 resin (Phenomenex). The mass
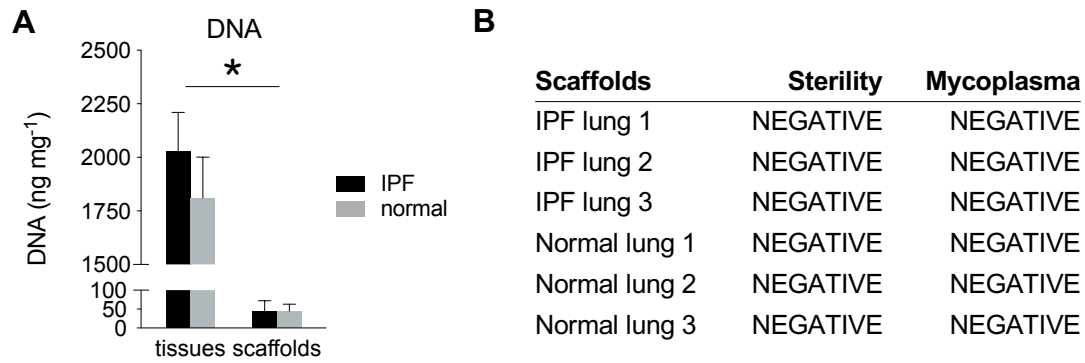
855   spectrometer was operated in data-dependent mode, with the Orbitrap operating at 60,000

856   FWHM and 15,000 FWHM for MS and MS/MS, respectively. The instrument was run with a 3

857   second cycle for MS and MS/MS. Advanced Precursor Determination was employed. Data were

858   searched using a local copy of Mascot (Matrix Science) with the following parameters: Enzyme:

859   Trypsin/P; Database: SwissProt Human (concatenated forward and reverse plus common

860   contaminants); Fixed modification: Carbamidomethyl (C); Variable modifications: Oxidation (M/P),

861   Acetyl (N-term), Pyro-Glu (N-term Q), Deamidation (N,Q); Mass values: Monoisotopic; Peptide

862   Mass Tolerance: 10 ppm; Fragment Mass Tolerance: 0.02 Da; Max Missed Cleavages: 2. Mascot

863   DAT files were parsed into Scaffold (Proteome software) for validation and filtering to create a

864   non-redundant list per sample. Data were filtered using at least 1% protein and peptide FDR, and

865   requiring at least two unique peptides per protein.

36

A

Lung donor characteristics	IPF	normal	*p*-value
Age (years)	61 ± 6	44 ± 17	0.18
Height (cm)	160 ± 5	173 ± 7	0.06
Weight (kg)	55 ± 12	81 ± 18	0.10
BMI (kg m^{-2})	21 ± 3	27 ± 6	0.22
Smoking history (pack years)	0	0	—
Lung allocation score	55.0 ± 25.1	0	**0.02** ◄

B

C

Classification	Normal	Mild	Moderate	Severe
Representative H&E staining	(250 µm)			
Fibrosis score	0	1	2	3
Histologic features	Normal lung or minimal fibrous thickening of bronchiolar walls or alveolar septa	Moderate thickening of walls or septa without obvious damage to lung architecture	Increased fibrosis with damage to lung structure and formation of fibrous bands or masses	Severe distortion of structure and large fibrous areas; "honeycomb lung"; or total fibrous obliteration

D

Analyzed in this study	Description	Quantity
Lungs	IPF	3
	normal	3
Lobes per lung	right middle lobe (RML)	1
Regions per right middle lobe	medial, lateral, peripheral	3
Samples per region	medial × 2, lateral × 2, peripheral × 2	2
Samples per lung	2 samples per region × 3 regions	6
Total IPF lung samples	6 samples per RML × 3 lungs	**18**
Total normal lung samples	6 samples per RML × 3 lungs	**18**

E

F

G

Supplementary Figure 1 | Characterization of human IPF and normal lung tissues. (**A**) Donor characteristics of IPF and normal lung tissues. (**B**) Representative chest radiographs of IPF and normal lung donors. Arrows indicate changed lung shape, decreased lung volume, and increased radiopacity consistent with pulmonary fibrosis. (**C**) Fibrosis scoring rubric used to assess the extent of architectural disruption and fibrosis in human lung tissues. (**D**) Overview of the description and quantity of tissue samples analyzed in this study. (**E**) Samples were collected from three regions (i.e., medial, lateral, peripheral) of right middle lobes. (**F**) Demonstration of quantitative image analysis method used for fibrosis scoring. For each fibrosis score, a weighted average is calculated from the ratios of the total area. Five high-power fields were analyzed per region, and an average fibrosis score was calculated for each region. (**G**) Fibrosis scores of all regions of IPF and normal lungs investigated in this study. Only regions of IPF lungs with fibrosis score ≥ 2 (red triangle) were investigated in this study. * $p < 0.001$.

A

B

Scaffolds	Sterility	Mycoplasma
IPF lung 1	NEGATIVE	NEGATIVE
IPF lung 2	NEGATIVE	NEGATIVE
IPF lung 3	NEGATIVE	NEGATIVE
Normal lung 1	NEGATIVE	NEGATIVE
Normal lung 2	NEGATIVE	NEGATIVE
Normal lung 3	NEGATIVE	NEGATIVE

Supplementary Figure 2 | Quality control assays of IPF and normal lung matrix scaffolds. Quantification of (**A**) DNA to confirm removal of nuclear material from IPF and normal lung matrix scaffolds. (**B**) Results of sterility and mycoplasma assays. Prior to use in studies, IPF and normal lung matrix scaffolds were tested for absence of bacteria and fungi. Scaffolds were also tested for absence of mycoplasma using MycoAlert PLUS Mycoplasma Detection Assay. * $p < 0.001$.

Antibody	Application	Vendor	Product number	Dilution
Rabbit anti-alpha smooth muscle actin	IHC–P	Cell Signaling Technology	19245	1 : 500
Rabbit anti-fibrillin 2	IHC–P	Sigma Life Science	HPA012853	1 : 50
Rabbit anti-Ki67	IHC–P	ThermoFisher Scientific	PA1-38032	1 : 500
Rabbit anti-laminin γ1	IHC–P	Abcam	ab233389	1 : 2000
Rabbit anti-matrix gla protein	IHC–P	LS Bio	LS-B14824	1 : 100
Rabbit anti-periostin	IHC–P	Abcam	ab14041	1 : 300

ELISA kit	Application	Vendor	Product number	
Human basic fibroblast growth factor	Cell culture media	R&D Systems	DFB50	
Human transforming growth factor β	Cell culture media	R&D Systems	DB100B	

Supplementary Table 1 | Antibodies and ELISA kits.

Gene	Forward primer	Reverse primer
GAPDH	TGCACCACCAACTGCTTAGC	GGCATGGACTGTGGTCATGAG
MMP2	CTTCCAAGTCTGGAGCGATGT	TACCGTCAAAGGGGTATCCAT
COL1A1	TCTGCGACAACGGCAAGGTG	GACGCCGGTGGTTTCTTGGT
LAMC1	TGGGCATTCTTCTGTCTGTACAA	GCCACCCATCCTCATCAATC
ACTA2	CCTGGCTTCGCTGTCTACCT	TTGCGGTGGACGATGGA
PDGFC	GGACTCAGGCGGAATCCAA	CTGAGGATCTTGTACTCCGTTCTG
YAP1	ACGTTCATCTGGGACAGCAT	GTTGGGAGATGGCAAAGACA
PRRX1	CAGATTGGTGGCTGTTAGATTGAA	GATGCACTTTTAGCACACATTTGTATT
PTEN	CAAGATGATGTTTGAAACTATTCCAATG	CCTTTAGCTGGCAGACCACAA

Supplementary Table 2 | Primers.

IPF lung donor demographics and clinical characteristics

Characteristics	Donor 1	Donor 2	Donor 3
Sex	Female	Male	Female
Age (years)	62	66	55
Height (cm)	163	163	155
Weight (kg)	59	64	42
BMI (kg m^{-2})	22	24	18
Smoking history (pack years)	0	0	0
Lung disease	IPF	IPF	IPF
Lung allocation score	36.1	83.5	45.5
Radiologic characteristics	UIP, reticular opacities	UIP, honeycombing	UIP, reticular opacities

NORMAL lung donor demographics and clinical characteristics

Characteristics	Donor 1	Donor 2	Donor 3
Sex	Female	Male	Male
Age (years)	24	56	52
Height (cm)	165	175	178
Weight (kg)	81	63	99
BMI (kg m^{-2})	30	20	31
Smoking history (pack years)	0	0	0
Lung disease	None	None	None
Lung allocation score	0	0	0
Radiologic characteristics	Abnormal basilar aeration	Cardiac enlargement	Trace pleural effusion

Supplementary Table 3 | Demographics and clinical characteristics of human lung donors. UIP, usual interstitial pneumonia.

Growth factor	Description	Concentration (pg mL^{-1})		Fold change from normal
		Normal tissue	IPF tissue	
TGF-β3	Transforming growth factor β3	ND	65.8	*
HB-EGF	Heparin-binding EGF-like growth factor	ND	4.2	*
IGFBP-1	Insulin-like growth factor binding protein 1	0.5	86.8	159.5 ▲
bFGF	Basic fibroblast growth factor	10.1	213.8	21.2 ▲
EG-VEGF	Endocrine gland-derived vascular endothelial growth factor	2.2	38.1	17.3 ▲
BDNF	Brain-derived neurotrophic factor	31.1	145.4	4.7 ▲
GDF-15	Growth differentiation factor 15	97.8	243.4	2.5 ▲
PDGF-AA	Platelet-derived growth factor AA	228.1	486.7	2.1 ▲
IGFBP-6	Insulin-like growth factor binding protein 6	123.0	228.5	1.9 ▲
HGF	Hepatocyte growth factor	13313.2	19831.9	1.5 ▲
VEGF	Vascular endothelial growth factor	135.9	158.8	1.2 ▲
EGF R	Epidermal growth factor receptor	17343.2	12828.8	0.7 ▼
OPG	Osteoprotegerin	60.8	33.8	0.6 ▼

Supplementary Table 4 | Quantification of growth factors in IPF and normal lung tissues. Growth factor concentrations were measured by multiplex growth factor array. Green arrow (▲) indicates positive fold change (increase) from normal in concentration of growth factors. Red arrow (▼) indicates negative fold change (decrease) from normal in concentration of growth factors. ND: not detected. * IPF-specific growth factor not detected in normal lung tissue.